A&A 609, A62 (2018)
DOI: 10.1051/0004-6361/201731255

Astronomy & Astrophysics

Dust reddening and extinction curves toward gamma-ray bursts at $z > 4$

J. Bolmer[1,2,3], J. Greiner[2], T. Krühler[2], P. Schady[2], C. Ledoux[1], N. R. Tanvir[4], and A. J. Levan[5]

[1] European Southern Observatory, Alonso de Córdova 3107, Vitacura, Casilla 19001, Santiago 19, Chile
e-mail: jbolmer@eso.org
[2] Max-Planck-Institut für extraterrestrische Physik, Giessenbachstraße, 85748 Garching, Germany
[3] Technische Universität München, Boltzmannstraße 2, 85748 Garching, Germany
[4] University of Leicester, Department of Physics and Astronomy and Leicester Institute of Space & Earth Observation, University Road, Leicester, LE1 7RH, UK
[5] Department of Physics, University of Warwick, Coventry, CV4 7AL, UK

Received 26 May 2017 / Accepted 20 September 2017

ABSTRACT

Context. Dust is known to be produced in the envelopes of asymptotic giant branch (AGB) stars, the expanded shells of supernova (SN) remnants, and in situ grain growth within the interstellar medium (ISM), although the corresponding efficiency of each of these dust formation mechanisms at different redshifts remains a topic of debate. During the first Gyr after the Big Bang, it is widely believed that there was not enough time to form AGB stars in high numbers, hence the dust at this epoch is expected to be purely from SNe or subsequent grain growth in the ISM. The time period corresponding to $z \sim 5{-}6$ is thus expected to display the transition from SN-only dust to a mixture of both formation channels as is generally recognized at present.
Aims. Here we aim to use afterglow observations of gamma-ray bursts (GRBs) at redshifts larger than $z > 4$ to derive host galaxy dust column densities along their line of sight and to test if a SN-type dust extinction curve is required for some of the bursts.
Methods. We performed GRB afterglow observations with the seven-channel Gamma-Ray Optical and Near-infrared Detector (GROND) at the 2.2 m MPI telescope in La Silla, Chile (ESO), and we combined these observations with quasi-simultaneous data gathered with the XRT telescope on board the *Swift* satellite.
Results. We increase the number of measured A_V values for GRBs at $z > 4$ by a factor of ~2–3 and find that, in contrast to samples at mostly lower redshift, all of the GRB afterglows have a visual extinction of $A_V < 0.5$ mag. Analysis of the GROND detection thresholds and results from a Monte Carlo simulation show that although we partly suffer from an observational bias against highly extinguished sight-lines, GRB host galaxies at $4 < z < 6$ seem to contain on average less dust than at $z \sim 2$. Additionally, we find that all of the GRBs can be modeled with locally measured extinction curves and that the SN-like dust extinction curve, as previously found toward GRB 071025, provides a better fit for only two of the afterglow SEDs. However, because of the lack of highly extinguished sight lines and the limited wavelength coverage we cannot distinguish between the different scenarios. For the first time we also report a photometric redshift of $z_{\rm phot} = 7.88^{+0.75}_{-0.94}$ for GRB 100905A, making it one of the most distant GRBs known to date.

Key words. galaxies: high-redshift – dust, extinction – techniques: photometric

1. Introduction

As a result of their high luminosities, gamma-ray bursts (GRBs) provide a powerful and unique probe to study the interstellar medium (ISM) out to very high redshifts, up to the epoch of reionization (e.g., Gehrels et al. 2009; Kumar & Zhang 2015). Shining through their host galaxies, deviations from their simple, smooth and featureless, intrinsic power-law spectra caused by dust, metals, or gas, allow detailed studies of the illuminated regions along the line of sight of their host galaxy and the intergalactic medium (IGM; Galama & Wijers 2001; Kann et al. 2006; Schady et al. 2007). Broadband photometric and spectroscopic observations of the GRB afterglow are now routinely used to measure metal, molecule, and dust column densities along with depletion patterns or dust-to-metal ratios to high accuracy (e.g., Ledoux et al. 2009; Krühler et al. 2013; De Cia et al. 2013; Sparre et al. 2014; Wiseman et al. 2017). Likewise, interstellar extinction curves have been tested out to very high redshifts (Zafar et al. 2011a; Greiner et al. 2011; Perley et al. 2011; Schady et al. 2012), including detections of the characteristic 2175 Å bump (Krühler et al. 2008; Zafar et al. 2012) as known from the Milky Way (MW) and the Large Magellanic Cloud (LMC) or more unusual features (Savaglio & Fall 2004; Perley et al. 2008; Fynbo et al. 2014), which might give new clues about dust production and properties throughout the Universe.

Measuring dust at high redshift comes with substantial observational biases. Firstly, while ≳90% of all *Swift*-detected GRBs (>1000) are detected and localized in X-rays with the *Swift*/XRT, only about 30% have a redshift estimate. Secondly, at redshifts $z > 2$ dust reddening forms an increasing hindrance in detecting the optical and near-infrared (NIR) afterglow. For instance, for a GRB at a redshift of $z = 4$, depending on the extinction law, a rest-frame $A_V = 1$ mag corresponds to an observer frame $A_V \sim 4{-}5$ mag, just due to redshifting the bandpass because the attenuation by dust usually increases from red to blue

wavelengths. Heavily obscured afterglows, the so-called *dark* GRBs, are generally found to occur in more massive and redder galaxies (Krühler et al. 2011a; Rossi et al. 2012; Perley et al. 2013; Hunt et al. 2014), and it was argued that these bursts were more likely to be missed in follow-up campaigns.

Various approaches were therefore made to create optically unbiased samples of GRBs that are representative of the whole population. Cenko et al. (2009) and Greiner et al. (2011) for example chose only those GRBs that were observed within a few hours after the *Swift*/BAT trigger by instruments dedicated to observe every GRB. These and similar approaches, such as the BAT6 sample (Salvaterra et al. 2012; Covino et al. 2013) or the TOUGH (Hjorth et al. 2012) and SHOALS (Perley et al. 2016a,b) surveys, find the percentage of dark GRBs to be around ~2040% without necessarily considering a potential evolution with redshift. Although much smaller (<100), these samples then reach a completeness in redshift of >90%. Furthermore, especially at even higher redshifts ($z > 3.5$), when optical and NIR SEDs and spectra are increasingly absorbed by the Lyα forest, additional absorption by dust can theoretically make a detection of the afterglow nearly impossible, even for 8 m class telescopes.

At redshifts ($z > 4-6$), when the Universe is thought to have been still too young to have formed AGB stars in high numbers, SNe are expected to be the main source of dust. However, it is still under debate how effectively dust is produced in the expanded shells of supernova (SN) and how high the contribution from AGB stars might be (Valiante et al. 2009; Hirashita et al. 2014). This is mainly because a high percentage of the SN produced dust might be destroyed by the reverse shock of the SN itself (Nozawa et al. 2007; Schneider et al. 2012a). It is therefore likely that a significant initial production of dust in SN ejecta is required to explain the increasing evidence of large dust masses and high star formation rates found in high redshift galaxies (e.g., through ALMA; Mancini et al. 2015; Watson et al. 2015b; Laporte et al. 2017). Dust production in SN ejecta is observed in some local SNe remnants (Gomez et al. 2012; Indebetouw et al. 2014; Matsuura et al. 2015; De Looze et al. 2017) and predicted by some analytical models (Schneider et al. 2012b; Silvia et al. 2012), which cover a broad range of possible dust survival rates or a significant contribution from subsequent grain growth in the ISM (Nozawa et al. 2012, 2015; Sarangi & Cherchneff 2013; Michałowski 2015).

The theoretical model from Todini & Ferrara (2001) shows that SN-origin dust would produce a characteristic extinction curve, which could be measured in absorption systems toward background sources such as quasars and GRBs. Indeed, Maiolino et al. (2004) reported evidence for the SN origin of dust in a quasar at redshift $z = 6.2$[1]. Similar evidence for extinction caused by SN synthesized dust was found in two GRB afterglows at a redshift of $z > 4.8$. While two different authors reached the same conclusion for GRB 071025 (Perley et al. 2010; Jang et al. 2011), the claim for SN-type dust in GRB 050904 is more controversial (Stratta et al. 2007, 2011; Zafar et al. 2010).

The aim of this paper is to provide a detailed and consistent study of the dust extinction properties in the afterglows of the most distant GRBs to find out about a potential evolution with redshift and whether a SN-like dust extinction curve is required for some of the bursts. The paper is arranged as follows: in Sect. 2 we describe the current sample of GRBs at $z > 4$. Section 3 presents our data analysis and reduction technique, and the main results are summarized in Sect. 4. Finally, we discuss the results and conclude in Sect. 5. Throughout the paper all magnitudes are given in the AB system and we adopt the convention that the GRB flux density is described by $F_\nu(t) \propto t^{-\alpha}\nu^{-\beta}$. Unless indicated otherwise, all errors are given at 1σ confidence.

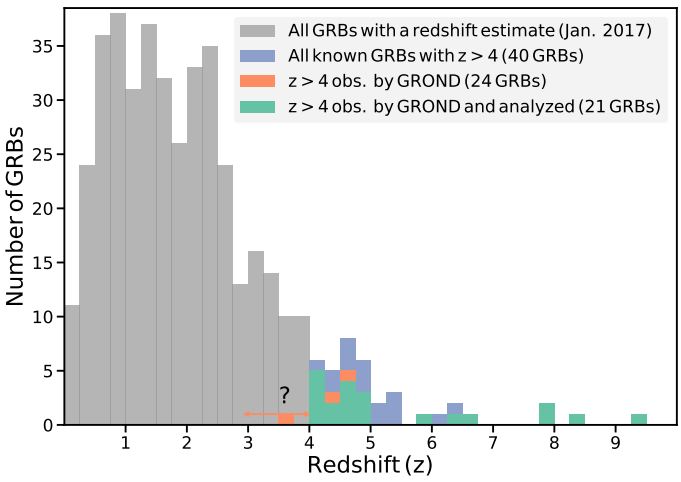

Fig. 1. Distribution of GRBs per redshift bin ($\Delta z = 0.25$) for the events discussed in this paper compared to all LGRBs with a reported redshift estimate (indicated in gray; including all events before January 2017). A total of 40 bursts (blue) have a well-derived redshift estimate of $z > 4$; 24 (orange) of these have been observed with GROND, from which 21 (green) are analyzed in this paper.

2. The sample

The GRB afterglow sample presented here is based on selecting all 40 observed events with a previously reported spectroscopic or photometric redshift of $z > 4$ (complete up until January 1, 2017; see Fig. 1)[2]. This sample is presented in Table 1, which is divided into three parts. Of these 40 GRBs, we were able to observe 24 via GROND, and of these, 21 GRBs (top part) were selected for our analysis and 3 GRBs (middle part) were excluded for reasons given below. The remaining 16 GRBs at $z > 4$ are listed in the bottom portion of the table. These either occurred before the GROND commissioning in 2007, were too far north to be observable from Chile (see Fig. 4), or were not observable with GROND because of bad weather (GRB 100513A). For each GRB, we give the coordinates of the NIR or optical afterglow, redshift, duration of the prompt emission (T_{90}), galactic foreground reddening E_{B-V} and hydrogen column density ($N_{\rm H}$), as well as the time after which we started observing the afterglow with GROND ($T_{\rm GROND}$). These properties of the sample are also visualized in Fig. 2.

Two of the GRBs observed by GROND lie close to the galactic plane and are behind high galactic dust and hydrogen column densities, namely GRB 080129 and GRB 131227A, and were thus excluded from the sample (see Fig. 4). Additionally, we excluded GRB 100518A because our analysis results in a photometric redshift of only $z_{\rm phot} = 3.50^{+0.50}_{-0.62}$ (see Sect. 3.4). Also only 4 out of the 21 analyzed GRBs are part of the unbiased GROND 4h sample, which contains all GRBs that have been observed within at least 4 h post trigger (Greiner et al. 2011). However, a large percentage of the bursts could be observed

[1] Hjorth et al. (2013) come to a different conclusion.

[2] This was performed on the basis of the public GRB table maintained by one of the co-authors: http://www.mpe.mpg.de/~jcg/grbgen.html; bursts classified as short and redshift values reported with a question mark were ignored.

Table 1. All GRBs with a spectroscopic or photometric redshift estimate of $z \geq 4$ (until the 1 of January 2017).

GRB (yymmdd#)	Right Ascension (J2000)	Declination (J2000)	Error	Redshift (z)	Ref.	T_{90} (s)	E_{B-V} (mag)	$N_{\rm H}$ (10^{21} cm^{-2})	$T_{\rm GROND}$ (h)
GRBs with $z > 4$ observed with GROND									
071025	+23:40:17.11	+31:46:42.74	0.″20	$4.88^{+0.35}_{-0.35}$	(1)	109 ± 2	0.06	0.55	21.69
080825B	+13:56:48.29	−68:57:18.57	0.″25	$4.31^{+0.14}_{-0.15}$	(2)	50	0.21	2.09	6.64
080913	+04:22:54.73	−25:07:45.98	0.″31	6.733	(3)	8 ± 1	0.04	0.33	0.10
080916C	+07:59:23.32	−56:38:17.92	0.″37	$4.28^{+0.6}_{-0.10}$	(1)	∼60	0.28	1.50	31.74
090205	+14:43:38.68	−27:51:10.10	0.″30	4.650	(4)	8.8 ± 1.8	0.10	0.80	6.39
090423	+09:55:33.27	+18:08:58.06	0.″29	8.26	(5)	10.3 ± 1.1	0.03	0.29	15.29
090429B	+14:02:40.10	+32:10:14.20	0.″30	$9.38^{+0.14}_{-0.32}$	(6)	5.5 ± 1.0	0.01	0.12	21.72
090516	+09:13:02.60	−11:51:14.90	0.″30	4.109	(7)	210 ± 65	0.04	0.45	14.60
100219A	+10:16:48.51	−12:34:00.50	0.″29	4.667	(8)	18.8 ± 5.0	0.07	0.65	9.20
100905A	+02:06:12.04	+14:55:45.80	0.″31	$7.88^{+0.75}_{-0.94}$	(1)	3.4 ± 0.5	0.05	0.54	16.02
111008A	+04:01:48.24	−32:42:32.87	0.″29	4.990	(9)	63.46 ± 2.19	0.01	0.10	6.43
120712A	+11:18:21.24	−20:02:01.41	0.″30	4.175	(10)	14.7 ± 3.3	0.04	0.36	9.25
120923A	+20:15:10.78	+06:13:16.30	0.″30	7.84	(11)	27.2 ± 3.0	0.13	0.98	18.95
130606A	+16:37:35.13	+29:47:46.61	0.″20	5.913	(12)	276.58 ± 19.31	0.02	0.20	6.43
131117A	+22:09:19.37	−31:45:44.22	0.″40	4.042	(13)	11.00 ± 3.16	0.02	0.15	0.05
140311A	+13:57:13.27	+00:38:32.11	0.″14	4.954	(14)	71.4 ± 9.5	0.03	0.25	11.72
140428A	+12:57:28.38	+28:23:06.88	0.″18	$4.68^{+0.52}_{-0.18}$	(1)	17.42 ± 5.90	0.01	0.09	2.05
140515A	+12:24:15.52	+15:06:16.62	0.″24	6.327	(15)	23.4 ± 2.1	0.02	0.23	13.76
140614A	+15:24:40.66	−79:07:43.20	0.″30	4.233	(16)	720 ± 120	0.11	0.82	0.54
151027B	+05:04:52.69	−06:27:01.07	0.″25	4.062	(17)	80.00 ± 35.78	0.18	0.58	7.76
151112A	+00:08:12.75	−61:39:48.47	0.″36	$4.27^{+0.24}_{-0.38}$	(1)	19.32 ± 31.24	0.01	0.18	10.43
GRBs with $z > 4$ observed with GROND that have been excluded from the sample									
080129	+07:01:08.20	−07:50:46.51	0.″28	4.349	(18)	48 ± 10	0.87	6.42	0.10
100518A	+20:19:09.33	−24:33:16.57	0.″28	$3.50^{+0.50}_{-0.62}$	(1)	25	0.07	0.63	17.13
131227A	+04:29:30.84	+28:52:58.92	0.″30	5.3	(19)	18.0 ± 1.6	0.90	1.51	21.39
All other GRBs with a redshift estimate of $z > 4$									
000131	+06:13:31.1	−51:56:41.7	1.″1	4.500	(20)	96.3	0.05	0.41	–
050502B	+09:30:10.1	+16:59:47.9	1.″4	$5.2^{+0.3}_{-0.3}$	(21)	17.5 ± 0.2	0.03	0.36	–
050505	+09:27:03.3	+30:16:24.2	1.″4	4.275	(22)	60 ± 2	0.02	0.17	–
050814	+17:36:45.4	+46:20:21.8	1.″4	$5.77^{+0.12}_{-0.12}$	(23)	65^{+40}_{-20}	0.02	0.23	–
050904	+00:54:50.9	+14:05:09.3	3.″5	6.295	(24)	225 ± 10	0.05	0.45	–
050922B	+00:23:13.4	−05:36:17.3	1.″7	4.5 ± 0.5	(25)	250 ± 20	0.03	0.31	–
060206	+13:31:43.4	+35:03:02.8	1.″5	4.048	(26)	7 ± 2	0.01	0.09	–
060223A	+03:40:49.6	−17:07:49.8	1.″5	4.406	(27)	11 ± 2	0.10	0.69	–
060510B	+15:56:29.2	+78:34:11.8	1.″5	4.941	(28)	276 ± 10	0.04	0.41	–
060522	+21:31:44.9	+02:53:09.9	1.″4	5.11	(29)	69 ± 5	0.05	0.42	–
060927	+21:58:12.0	+05:21:49.0	1.″6	5.467	(30)	22.6 ± 0.3	0.05	0.46	–
100302A	+13:02:03.8	+74:35:23.7	1.″5	4.813	(31)	17.9 ± 1.7	0.02	0.19	–
100513A	+11:18:26.8	+03:37:40.8	1.″4	4.772	(32)	84 ± 21	0.05	0.42	–
120521C	+14:17:08.8	+42:08:41.5	1.″6	6.0	(33)	26.7 ± 4.4	0.01	0.11	–
140304A	+02:02:34.3	+33:28:25.7	1.″5	5.283	(34)	15.6 ± 1.9	0.07	0.60	–
140518A	+15:09:00.6	+42:25:05.7	2.″7	4.707	(35)	60.5 ± 2.4	0.01	0.15	–

Notes. Columns 5–10 are the redshift (photometric when given with errors, spectroscopic otherwise), corresponding reference, time interval T_{90} over which 90% of the total background-subtracted counts are observed (GRBs with $T_{90} > 2$ s are classified as long gamma-ray bursts (LGRBs)), galactic foreground reddening from Schlafly & Finkbeiner (2011), as retrieved from the NASA Extragalactic database (NED, http://irsa.ipac.caltech.edu/applications/DUST/), total galactic neutral hydrogen column density provided by Kalberla et al. (2005), and start of the GROND observations in hours after the GRB Trigger (rounded to two decimal places).

References. (1) this work; (2) Krühler et al. (2011b); (3) Patel et al. (2010); (4) Fugazza et al. (2009); (5) Tanvir et al. (2009); (6) Cucchiara et al. (2011); (7) de Ugarte Postigo et al. (2009); (8) Mao et al. (2012); (9) Wiersema et al. (2011); (10) Xu et al. (2012); (11) Tanvir et al. (2017); (12) Xu et al. (2013); (13) Hartoog et al. (2013); (14) Tanvir et al. (2014); (15) Chornock et al. (2014); (16) Krühler et al. (2014); (17) Xu et al. (2015); (18) Greiner et al. (2009c); (19) Cucchiara & Cenko (2013); (20) Andersen et al. (2000); (21) Afonso et al. (2011); (22) Berger et al. (2006); (23) Curran et al. (2008); (24) Kawai et al. (2006); (25) Schulze et al. (2015); (26) Fynbo et al. (2006); (27) Chary et al. (2007); (28) Price et al. (2007); (29) Cenko et al. (2006); (30) Ruiz-Velasco et al. (2007); (31) Chornock et al. (2010); (32) Cenko et al. (2010b); (33) Laskar et al. (2014); (34) Jeong et al. (2014); (35) Chornock et al. (2014).

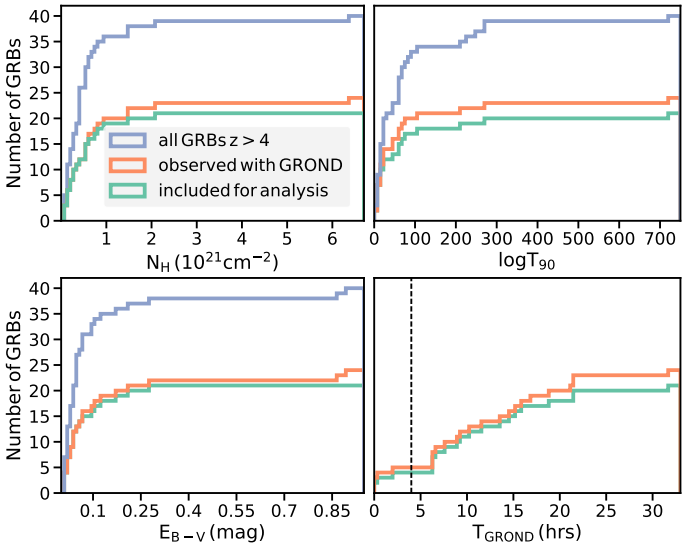

Fig. 2. Cumulative distribution of the basic properties of the GRBs at $z > 4$. Shown are the galactic foreground reddening E_{B-V} and hydrogen column density $N_{\rm H}$, as well as the duration of the prompt emission T_{90} and the time of the first GROND observation $T_{\rm GROND}$. With two exceptions, all GRBs are behind modest galactic dust and hydrogen column densities (*left panels*). The value T_{90} is between 2 and 300 s for all of the GRBs with the only outliner being GRB 140614A with 720 s (*top right panel*). The majority of the GRBs were observed by GROND between 4 to 18 h after the trigger; only 6 are part of the unbiased GROND 4h sample (Greiner et al. 2011) (*bottom right panel*).

between 4 and 18 h after their detection, during the first night in La Silla (Chile) usually providing a high chance of reliable detections in most of the seven GROND filter bands. Only three bursts (GRB 071025, 080916C, and 090429B) could not be observed with GROND during the first night of their trigger, mainly due bad weather in La Silla. Finally, although all 24 GRB afterglows observed with GROND were also observed and detected with *Swift*/XRT, the prompt emission of three of these was initially detected by instruments on other satellites (GRB 080825B: Agile/GRID, GRB 080916C: *Fermi*/GBM+LAT, and GRB 100518A: INTEGRAL/IBIS).

3. Data reduction and analysis

For the aim of this paper all GRBs with a redshift of $z > 4$ and observed by GROND and *Swift*/XRT, were analyzed to create broadband SEDs to measure dust column densities and test extinction curves along their line of sight.

3.1. X-ray data analysis

The XRT X-ray light curves and spectra of the afterglow were taken from the automated data products provided by the public *Swift*/XRT repository (Evans et al. 2009). To ensure that there were at least 20 counts per bin, we further regrouped the spectral data from 0.3–10 keV in the chosen time interval from the photon counting mode (PC) alone with the *grappha* task from the `HEAsoft` package and the response matrices from CALDB (Version `v20120209`); this also ensured that bad columns could be ignored. In cases where no X-ray data were available simultaneously to the GROND observations, the XRT spectra were additionally flux normalized to the mid-time of the chosen GROND exposure using the temporal decay model, which best fit the XRT light curve. The common reference time was generally chosen to be after any optical rise/late-time re-brightening, steep decay, or plateau phase, at least in those cases where such a distinction was possible. We also avoided selecting time intervals from periods of X-ray flares or spectral evolution, i.e., time intervals of changing temporal decay.

3.2. Near-infrared and optical data analysis

Image reduction and photometry of the GROND observations were carried out with the standard *Image Reduction and Analysis Facility* tasks (IRAF; Tody 1993), as described in Krühler et al. (2008). The absolute calibration of the GROND observations in $g'r'i'z'$ was carried out with stars observed in the Sloan Digital Sky Survey (SDSS). In cases where the GRB was not in a field covered by the SDSS, an SDSS field and the GRB field were observed consecutively during photometric conditions to cross-calibrate the zero points. The absolute NIR calibration in $JHK_{\rm s}$ was performed using the Two Micron Sky Survey (2MASS; Skrutskie et al. 2006) stars within the field of the GRB. This method results in typical systematic errors of 0.03 mag for the $g'r'i'z'$ bands, 0.05 mag for the JH bands, and 0.07 mag for the $K_{\rm s}$ band. Finally, before the fitting process, all magnitudes were corrected for the galactic foreground reddening according to the values given by Schlafly & Finkbeiner (2011) and listed in Table 1. The complete set of GROND photometry for the GRBs at $z > 4$ is given in Table D.1.

As an example, the optical, NIR, and XRT X-ray light curves of GRB 100905 are shown in Fig. 5. The light curves of all other GRBs are moved to the Appendix (Fig. B.1 to Fig. B.21), where we also describe the light-curve analysis in more detail and list the best-fit models in Table C.1.

3.3. Position of the near-infrared and optical afterglow

The position of the afterglow was determined by using the USNO or SDSS field stars as astrometric reference. For the majority of the GRBs we used the GROND z' band observations and averaged over all detections. For GRB 090423 and 100905A, which were not detected in z', we used the 2MASS field stars in the GROND J band. This method results in a typical absolute error of 0.″3 in each coordinate. For the bursts that were observed but not detected by GROND, namely GRB 090429, 120923A, and 131227A, we collected coordinates from the literature (Cucchiara et al. 2011; Cucchiara & Cenko 2013; Tanvir et al. 2017). For the rest of the bursts, in Table 1 we simply list the XRT positions[3], which are typically good to ≈2″; for GRB 000131 we use the position given by Andersen et al. (2000).

3.4. Photometric redshifts

From the 24 GRBs observed with GROND, 15 have a spectroscopically measured redshift. All the other GRBs have photometric redshift measurements from the afterglow, of which some are studied in detail in refereed publications and others are only rough estimates that were published in GCNs. For the latter we here provide new and more precise constraints based on carefully analyzed and calibrated GROND data.

The photometric redshift for GRB 080825B of $z_{\rm phot} \sim 4.3$ was determined by Krühler et al. (2011b) based on the Lyman-break technique, using multi-band photometry from GROND and UVOT. We used that same, robust and reliable method to

[3] Taken from `http://www.swift.ac.uk/xrt_positions/`

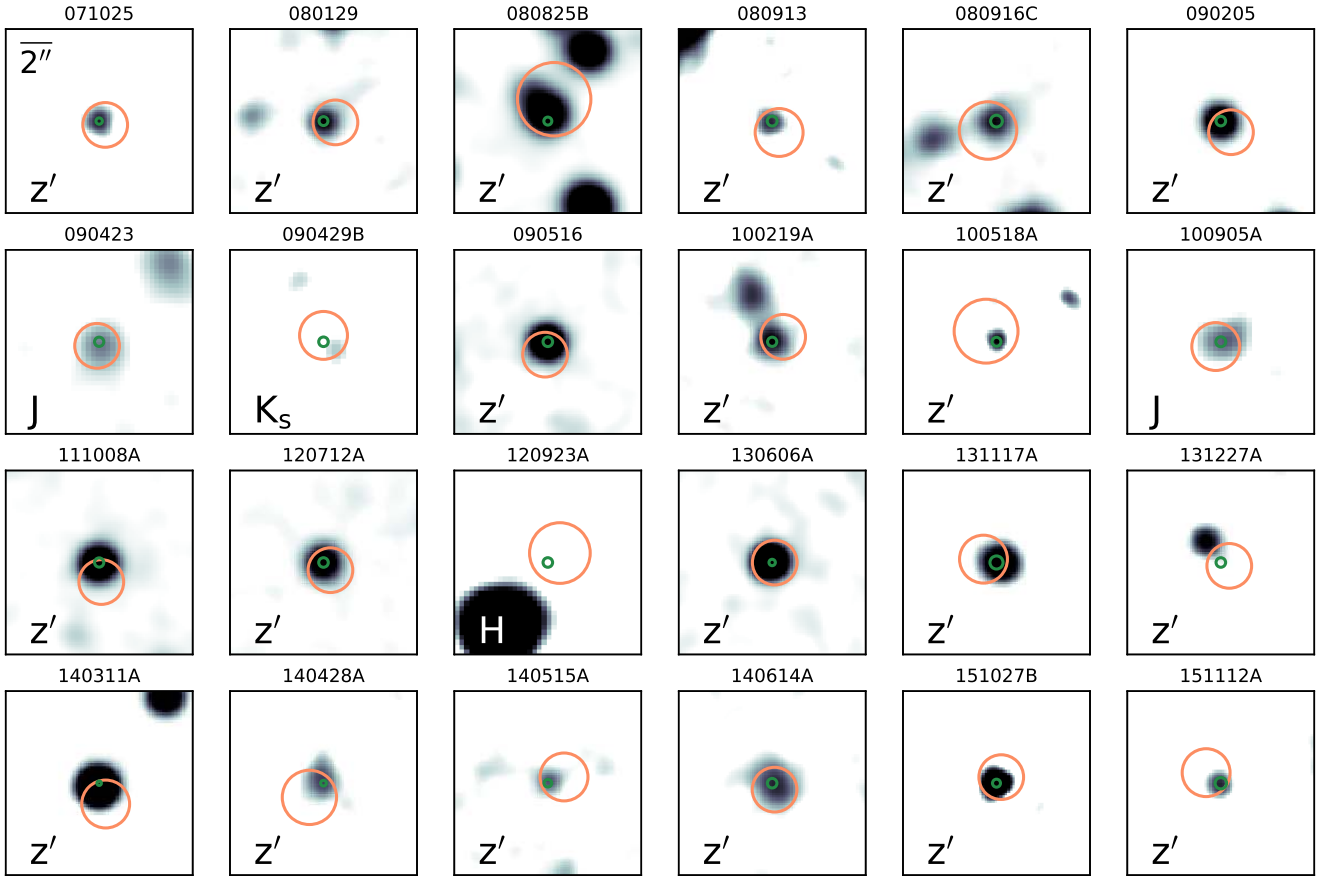

Fig. 3. Thumbnails for the 24 GRBs observed with GROND. The orange circles represent the *Swift*/XRT 90% error circles as taken from www.swift.ac.uk/xrt_positions/, and the green circles show the position of the NIR or optical afterglow as given in Table 1. A 2″ scale bar is shown in the top left plot for GRB 071025 and the particular GROND filter is denoted in the bottom left corner of each finding chart. With the exception of GRBs 090429B, 120923A, and 131227A, we were able to detect the NIR or optical counterpart with GROND.

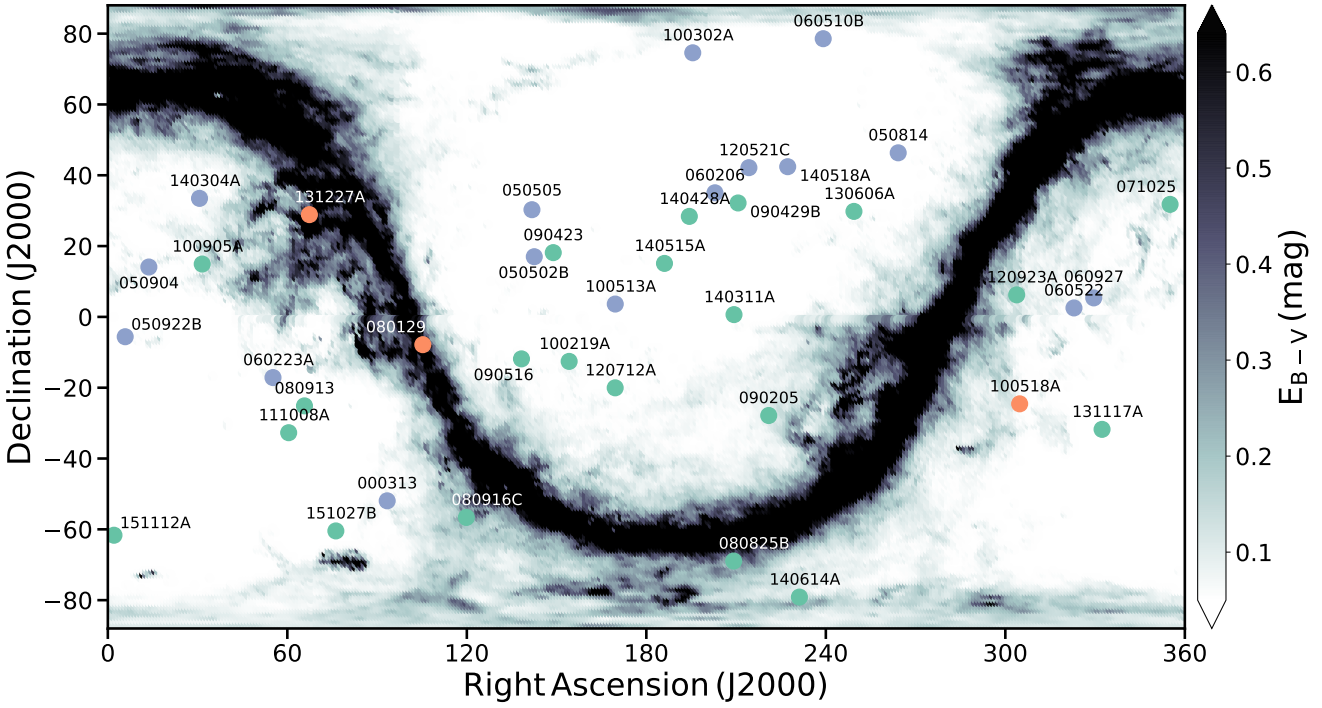

Fig. 4. All-sky map of the galactic dust reddening E_{B-V} as given by Schlafly & Finkbeiner (2011). The GRBs analyzed here are indicated in green. Those indicated in orange were excluded from the sample and those colored in blue are all other known GRBs with a redshift of $z > 4$. The sky above Dec > 44° cannot be observed from La Silla (Chile), where GROND is mounted at the 2.2 m MPI telescope.

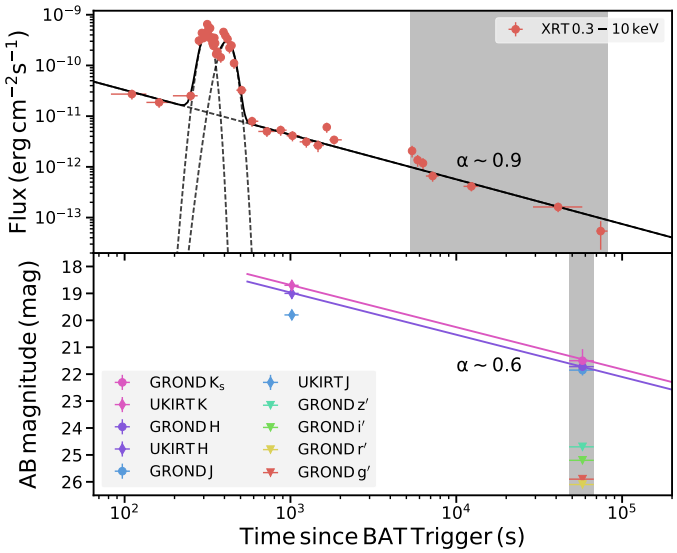

Fig. 5. Near-infrared and optical and XRT X-ray light curves of GRB 100905A. In addition to the GROND detections and upper limits we also plot UKIRT J-, H- and K-band magnitudes as reported by Im et al. (2010). The XRT light curve shows some flaring activity between T_0 + 300 and T_0 + 600 s and is otherwise best fit with a single power law and a temporal decay slope of $\alpha_X \sim 0.9$. The GROND and UKIRT K- and H-band light curves indicate a temporal decay slope of $\alpha_o \sim 0.6$. The time intervals used to created the quasi-simultaneous broadband SED are indicated in gray.

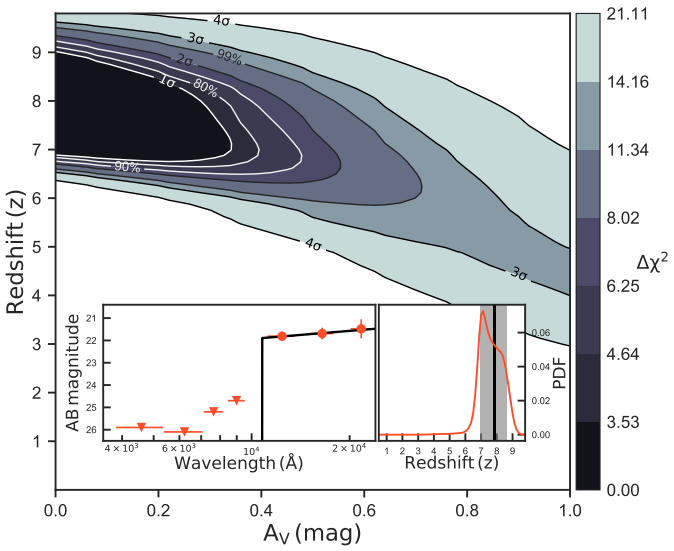

Fig. 6. Contour plot of the $\Delta\chi^2$ values for each of fitted host-intrinsic visual extinction A_V and redshift (z) parameters for the best-fit power-law index of $\beta = 0.45$. For three degrees of freedom, the significance levels of 1σ (68.27%), 2σ (95.45%), 3σ (99.73%), and 4σ (99.99%) correspond to $\Delta\chi^2 = 3.53$, 8.02, 11.35, and 21.11, respectively. As shown in the *left inset*, the GROND SED is best fit with the SMC extinction curve, a power-law slope of $\beta = 0.45$, no dust extinction ($A_V = 0.00$ mag), and a photometric redshift of $z_{\rm phot} = 7.88^{+0.75}_{-0.94}$. In the *inset on the right* we also show the corresponding redshift probability density function. The gray shaded area indicates the 1σ confidence interval.

determine and confirm photometric redshifts of $z_{\rm phot} > 4$ for GRB 071025, 080916C, 100905A, 140428A, and 151112A. For GRB 100518A, we cannot confirm the previously determined redshift of $z_{\rm phot} > 4$. As already noted by Kann et al. (2013), for GRB 131227A a detection with GROND is ambiguous, and finally, for GRB 090429B we used the photometric redshift determined by Cucchiara et al. (2011). All spectroscopic and photometric redshifts and the corresponding references are listed in Table 1.

Since this is the first time we publish the GROND data and a photometric redshift for GRB 100905A, we briefly describe the burst in the following subsection. Details and plots regarding the other five bursts are moved to the Appendix.

3.5. GRB 100905A

Swift/BAT triggered on GRB 100905A on September 6, 2010 at T_0 = 15:08:14 UT (MJD = 55 444.63072) with a duration of T_{90} = 3.4 ± 0.5 s (Barthelmy et al. 2010; Marshall et al. 2010). The XRT started observing the field around 100 s after the trigger. The UVOT observations only lead to upper limits (Siegel & Marshall 2010). We started observing the field with GROND at around 13 h after the BAT trigger and detected the afterglow in J, H, and K_s at a common position of RA, Dec = +02:06:12.04, +14:55:45.80 with an absolute accuracy of 0.″31 in each coordinate (as for all of the other GRBs, the magnitudes and upper limits are given in Table D.1). The afterglow was also detected in J, H, and K by Im et al. (2010) using the United Kingdom Infra-Red Telescope (UKIRT). The XRT X-ray, optical, and NIR light curves are shown in Fig. 5. Besides some flaring activity between T_0 + 300 and T_0 + 600 s, the XRT light curve is best fit with a single power-law and a temporal decay index of $\alpha_x = 0.88 \pm 0.03$. When compared to the UKIRT observations, our GROND magnitudes indicate a somewhat weaker fading of the optical and NIR afterglow ($\alpha_o = 0.60 \pm 0.06$), when assuming a singe power-law decay.

Using the method presented in Krühler et al. (2011b), we determine a photometric redshift of $z_{\rm phot} = 7.88^{+0.75}_{-0.94}$, when fitting the GROND magnitudes with a single power law, which is reddened by dust following the Small Magellanic Cloud (SMC) extinction law. The big errors are the result of the missing wavelength coverage between the z' and J band. The corresponding $\Delta\chi^2$ contours, given the best-fit spectral slope of $\beta = 0.45$, as well as the GROND SED and the redshift probability density function, are shown in Fig. 6. Using only the GROND magnitudes we find no evidence for absorption by dust ($A_V = 0.00^{+0.27}_{-0.00}$ mag).

So far, no robust redshift measurement for this event is reported in the literature, but, if correct, it would make GRB 100905A one of the most distant GRBs known to date[4].

The very high redshift interpretation is consistent with the non-detection of a host galaxy in deep NIR imaging from the *Hubble* Space Telescope. In a total of 10423 s of exposure in the *WFC3/F140W* filter, no host is detected down to a 3σ limiting magnitude of $F140W > 28.5$ mag$_{\rm AB}$. These faint magnitudes are characteristic for high-z GRB hosts in general (Tanvir et al. 2012; McGuire et al. 2016) and would be somewhat unexpected for a lower redshift ($z \sim 2$) galaxy hosting a dust-extinguished GRB (Krühler et al. 2011a).

3.6. Spectral energy distribution fitting

In theory, GRB afterglow spectra are featureless and non-thermal, synchrotron spectra made up of a number of connected

[4] Starling et al. (2013) assumed a photometric redshift of $z = 7$, based on private communication with Im. et al. and Littlejohns et al. (2013) list $z \sim 7.25$ without giving a reference.

power laws. Observations in the X-ray, optical, and NIR regime, typically sample the same portion of the synchrotron spectrum, i.e., a single power law describes the X-ray to NIR SED; in some case, however, the synchrotron cooling frequency lies between the X-ray and NIR spectral range, producing a change in spectral slope at higher energies. Hence, after rescaling XRT and GROND data to a common reference time and correcting the GROND magnitudes for the foreground reddening given in Table 1, the NIR to X-ray broadband SEDs were fitted in XSPEC with the combined model of PHABS·ZPHABS·ZDUST·POW and PHABS·ZPHABS·ZDUST·BKNPOW. The redshift was fixed to that obtained from spectroscopic measurements of the afterglow, host, or photometric dropout, in this order of priority, either from literature or determined in this work. The galactic foreground hydrogen column densities were fixed to the values listed in Table 1 and in the case of a broken power law, the difference in slope between X-ray, optical, and NIR wavelengths was fixed to 0.5, according to the standard fireball model for the slope difference around the cooling frequency and in line with the majority of GROND-measured SEDs Greiner et al. (2011). Filters blueward of Lyα at the GRB redshift were ignored owing to additional absorption from the Lyα forest. All other parameters were left free and χ^2 was minimized when fitting each of the three extinction curves featured in the ZDUST model, namely those for the SMC and LMC as well as the MW, with a single or a broken power law. Additionally, for the burst showing evidence for dust extinction (i.e., $A_V > 0.1$ mag) we also fitted the model from Todini & Ferrara (2001) & Maiolino et al. (2004) for an extinction curve caused by SN synthesized dust. Its most characteristic feature is the flattening between 3000 and 1700 Å followed by a steep decline (see Fig. 2 in Maiolino et al. 2004). The reason we explored only one out of various extinction curves proposed for SN-type dust is discussed in Sect. 5.

Especially for GRBs at high redshift, when more and more of the GROND bands are affected by absorption caused by the Lyα forest, it is not feasible to fit more general extinction curves that have more free parameters, such as R_V and the prominence of the 2175 Å feature; for example, the extinction curves proposed by Cardelli et al. (1989) or Fitzpatrick & Massa (1986, hereafter FM)[5]. This is also the reason for including quasi-simultaneous XRT data to fit the SED, so that the mostly unabsorbed and well-covered X-ray spectrum for energies $E > 0.8$ keV allows us to constrain better the spectral index; this means that we reduce the uncertainty for the optical and NIR spectral slope to the question of whether a spectral break of 0.5 is required or not.

The absorption of the X-ray spectrum by medium weight metals at energies below $E < 0.8$ keV is modeled with the XSPEC models PHABS & ZPHABS. However, the resulting host intrinsic hydrogen column densities $N_{\rm H,X}$ is not discussed further here because we refer to the recent findings by Buchner et al. (2017), who have used a more sophisticated model to fit XRT spectra. These authors find the distribution of $N_{\rm H,X}$ to be consistent with sources being randomly distributed in an ellipsoidal gas cloud. This is in contrast to previous studies by, for example, Starling et al. (2013) or Campana et al. (2015), who find a positive dependence with redshift (as we do here), which could be interpreted as increasing absorption from the IGM with distance.

[5] Also, Zafar et al. (2011a) found only 4 out of 42 GRBs to be better fit with the FM extinction law.

3.7. Additional data for GRBs at $z > 4$ not observed or detected with GROND

Our GROND observations for GRB 090429B only led to upper limits in all seven bands, and we therefore carried out the analysis on *Gemini*/NIRI JH and K-band data published in Cucchiara et al. (2011). We did not carry out the fit for GRB 120923A ourselves, but used the visual extinction of $A_V = 0.06$ mag determined by Tanvir et al. (2017), who have used a very similar method for fitting simultaneous XRT and *Gemini-N*/NIRI data. Additionally, for two of the bursts that were not observed by GROND, namely GRB 100513A and 140304A, we used PAIRITEL JHK and RATIR $grizJH$ data for the analysis, respectively. So in total we analyzed and fitted 22 GRB broadband SEDs, 19 with GROND and 3 with optical and NIR data from different instruments. For the rest of the GRBs at $z > 4$, we collected A_V measurements from the literature if available; these measurements are listed in Table 3.

4. Results

The results, i.e., the best-fit models and parameters, from fitting the combined NIR, optical, and X-ray SEDs with the local extinction curves are summarized in the top portion of Table 2 and a plot containing all the SEDs is shown in Fig. 7. As mentioned above, the SEDs of the 10 GRBs that show evidence for a small to medium amount of dust ($A_V > 0.1$ mag) were also fitted with the SN extinction curve. These SEDs are additionally plotted in Fig. 8, in comparison to the best results from the local extinction curves (zoomed into the optical and NIR regime; the full plot is displayed in Fig. C.1). The corresponding parameters are given in the bottom portion of Table 2.

With these measurements we increase the number of determined A_V values for GRBs at $z > 4$ by a factor of ~2–3. As previously observed for GRBs at lower redshift, the local extinction curves provide a good fit to the data, with the featureless SMC extinction curve usually best describing the observed magnitudes (Greiner et al. 2011; Zafar et al. 2011a). We find that from the 22 modeled GRBs at $z > 4$, 16 are best fit with the SMC and only 6 are best fit with the LMC or MW extinction curve. In contrast to other samples with GRBs at mostly $z < 4$, however, we find that all of the GRBs are only behind small to medium dust column densities ($A_V < 0.5$ mag) within their host galaxies line of sight, which is also true for the values collected from the literature (see Table 3). The distribution of our best-fit A_V values compared to those from the unbiased samples from Greiner et al. (2011) and Covino et al. (2013) and the data from Zafar et al. (2011a), based on the GRB sample from Fynbo et al. (2009), is shown in Fig. 9. While all of these samples include a ~20% of GRBs with $A_V > 0.5$ mag (and ~3–5% with $A_V > 1.5$ mag), only ~20% of our GRBs at redshift $z > 4$ have a visual extinction of $0.2 < A_V < 0.5$ mag and the remaining ~80% have $A_V < 0.2$ mag. A two-sample Kolmogorov-Smirnov test returns a rejection probability of $p \sim 68\%$ for the null hypothesis that the A_V values from our GRBs at $z > 4$ and those from Greiner et al. (2011) are drawn from the same sample.

Considering the 10 SEDs that were also fitted with the SN extinction curve, we find that, besides GRB 090205 and 090516, the goodness of fit is comparable to the result from the local extinction curves, while for two of the bursts, GRB 140428A and 151027B, the SN extinction curve provides a better fit to the data. In case of GRB 140428A, the somewhat flat SED between the H and z' band can be identified with the flattening between (rest-frame) 3000 and 1700 Å of the SN extinction curve

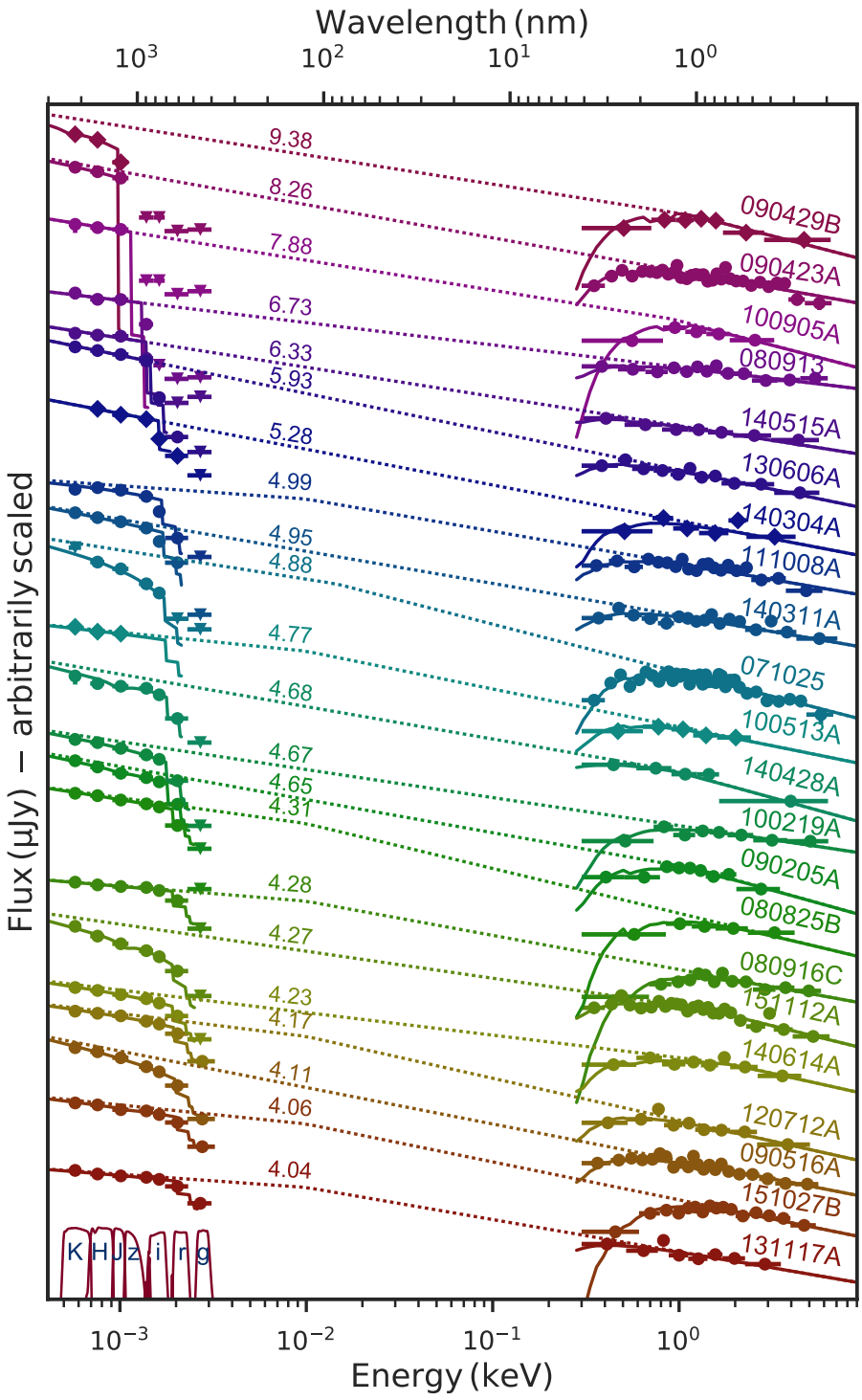

Fig. 7. Spectral energy distribution for the 22 GRBs analyzed in this paper with increasing redshift from the bottom to top (as labeled). Data for GRBs detected with GROND are plotted with circles, data from other instruments with diamonds. The X-ray spectrum, if not available simultaneously to the optical and NIR data, was flux normalized to the mid-time of the chosen GROND exposure. Dashed lines indicate the unabsorbed best-fit models. Solid lines indicate the best-fit model including absorption: in the X-rays due to galactic plus host intrinsic absorption by medium weight metals; in the optical and NIR range due to host intrinsic absorption by dust (the data were corrected for galactic foreground reddening beforehand). The flux on the y-axis is completely arbitrary to get a better visualization. In the left corner at the bottom of the plot we also show the GROND filter curves.

($\chi^2_{\rm red}$ = 1.16) or as a small (rest-frame) 2175 Å feature when fitting the MW extinction curve ($\chi^2_{\rm red}$ = 1.44). This result is consistent with that from fitting the GROND SED to determine a photometric redshift, where we also find that the SN extinction curve is in better agreement with the data (see Appendix D). For GRB 151027B we find $\chi^2_{\rm red}$ = 1.05 for the SN extinction curve, compared to $\chi^2_{\rm red}$ = 1.17 for the LMC extinction curve. However, because of the small amount of dust ($A_V \sim 0.10$ mag), it is hard to distinguish between the specific features of those extinction curves (see Fig. 8). Also, although the SMC extinction curve provides the best fit ($\chi^2_{\rm red}$ = 1.11), GRB 071025 can also be well modeled with the SN extinction curve ($\chi^2_{\rm red}$ = 1.16), which is in accordance with the results from Perley et al. (2010) and Jang et al. (2011) and with our result from fitting the GROND SED to determine a photometric redshift (see Appendix D). GRB 071025 is, aside from GRB 151112A ($A_V \sim 0.5$ mag), also the burst for which we find the highest visual extinction (SMC: $A_V \sim 0.45$ mag, SN: $A_V \sim 0.57$ mag).

5. Discussion and conclusions

We have analyzed a sample of 40 GRBs at $z > 4$, of which 22 were used to measure the host intrinsic visual extinction A_V and study the shape of the dust extinction curves toward

Table 2. Summary of the best-fit models and parameters of the 22 GRBs analyzed in this paper.

GRB (yymmdd#)	Redshift fixed to	Model	Ext. Curve	β_o [a]	A_V (mag)	E_{break} (keV)	Norm. (keV/cm^2/s/keV)	χ^2 (d.o.f.)	χ^2_{red}	T_{SED} [b] (h)
071025	4.900	bknpow	smc	$0.77^{+0.17}_{-0.08}$	$0.45^{+0.13}_{-0.14}$	1.45×10^{-2}	2.78×10^{-4}	40.1 (36)	1.11	22.4
080825B	4.310	bknpow	smc	$0.67^{+0.19}_{-0.03}$	$0.05^{+0.02}_{-0.02}$	9.93×10^{-3}	1.82×10^{-3}	2.9 (5)	0.58	12.4
080913	6.733	pow	smc[d]	$0.59^{+0.02}_{-0.02}$	$0.00^{+0.00}_{-0.00}$	.....	1.02×10^{-3}	9.9 (12)	0.83	0.2
080916C	4.280	bknpow	smc[d]	$0.40^{+0.18}_{-0.02}$	$0.01^{+0.03}_{-0.01}$	9.99×10^{-3}	1.15×10^{-3}	12.3 (13)	0.95	32.6
090205A	4.650	bknpow	lmc	$0.88^{+0.04}_{-0.24}$	$0.14^{+0.04}_{-0.05}$	$1.24 \times 10^{+0}$	1.61×10^{-4}	9.2 (9)	1.02	7.1
090423A	8.260	pow	smc	$0.88^{+0.04}_{-0.04}$	$0.08^{+0.09}_{-0.09}$	.....	4.37×10^{-5}	28.0 (31)	0.90	17.3
090429B[c]	9.380	bknpow	lmc	$0.77^{+0.07}_{-0.29}$	$0.36^{+0.22}_{-0.21}$	$1.21 \times 10^{+0}$	1.81×10^{-4}	2.2 (4)	0.55	2.9
090516A	4.109	pow	smc	$0.97^{+0.02}_{-0.02}$	$0.19^{+0.03}_{-0.03}$	.....	1.62×10^{-4}	17.1 (23)	0.74	15.3
100219A	4.667	pow	smc	$0.74^{+0.03}_{-0.03}$	$0.15^{+0.04}_{-0.05}$	.....	2.22×10^{-4}	4.2 (9)	0.47	11.4
100513A[c]	4.772	bknpow	smc	$0.50^{+0.09}_{-0.35}$	$0.04^{+0.24}_{-0.04}$	9.94×10^{-3}	6.30×10^{-3}	0.8 (3)	0.27	1.0
100905A	7.880	bknpow	mw[d]	$0.79^{+0.35}_{-0.33}$	$0.00^{+1.49}_{-0.00}$	9.30×10^{-1}	4.10×10^{-5}	0.9 (3)	0.30	16.0
111008A	4.990	bknpow	smc	$0.35^{+0.20}_{-0.01}$	$0.13^{+0.03}_{-0.07}$	9.98×10^{-3}	9.28×10^{-3}	27.0 (19)	1.42	6.8
120712A	4.175	bknpow	smc	$0.61^{+0.24}_{-0.02}$	$0.08^{+0.03}_{-0.08}$	9.99×10^{-3}	9.49×10^{-4}	9.5 (9)	1.06	10.6
130606A	5.931	pow	smc[d]	$1.01^{+0.02}_{-0.02}$	$0.00^{+0.02}_{-0.00}$	.....	1.83×10^{-4}	7.1 (11)	0.65	8.4
131117A	4.042	bknpow	smc	$0.35^{+0.14}_{-0.02}$	$0.03^{+0.03}_{-0.03}$	1.00×10^{-2}	2.51×10^{-2}	10.4 (8)	1.30	0.1
140304A[c]	5.283	pow	smc[d]	$0.95^{+0.04}_{-0.03}$	$0.01^{+0.05}_{-0.01}$	.....	2.04×10^{-4}	10.4 (6)	1.33	14.4
140311A	4.954	pow	smc	$0.85^{+0.02}_{-0.02}$	$0.07^{+0.03}_{-0.03}$	.....	2.08×10^{-4}	20.6 (17)	1.21	9.8
140428A	4.680	bknpow	mw	$0.86^{+0.09}_{-0.30}$	$0.30^{+0.32}_{-0.23}$	9.33×10^{-1}	1.25×10^{-4}	7.2 (5)	1.44	2.6
140515A	6.327	pow	smc[d]	$0.77^{+0.04}_{-0.03}$	$0.00^{+0.10}_{-0.00}$	.....	1.36×10^{-4}	3.7 (6)	0.62	14.6
140614A	4.233	bknpow	smc	$0.60^{+0.05}_{-0.05}$	$0.11^{+0.17}_{-0.05}$	$1.89 \times 10^{+0}$	2.83×10^{-4}	5.2 (8)	0.65	4.1
151027B	4.062	bknpow	lmc	$0.50^{+0.08}_{-0.02}$	$0.10^{+0.05}_{-0.06}$	1.00×10^{-2}	4.21×10^{-3}	18.7 (16)	1.17	8.8
151112A	4.270	bknpow	lmc	$0.71^{+0.05}_{-0.06}$	$0.50^{+0.21}_{-0.11}$	$1.36 \times 10^{+0}$	2.59×10^{-4}	21.4 (25)	0.86	11.4
071025	4.900	bknpow	sn	$0.80^{+0.16}_{-0.07}$	$0.57^{+0.18}_{-0.21}$	9.99×10^{-3}	3.40×10^{-4}	41.9 (36)	1.16	22.4
090205	4.900	pow	sn	$0.90^{+0.03}_{-0.03}$	$0.10^{+0.03}_{-0.03}$	...	1.31×10^{-4}	13.7 (10)	1.37	7.1
090429B[c]	9.380	bknpow	sn	$0.72^{+0.06}_{-0.27}$	$0.19^{+0.22}_{-0.14}$	$1.19 \times 10^{+0}$	1.75×10^{-4}	2.2 (4)	0.55	2.9
090516A	4.109	pow	sn	$0.98^{+0.02}_{-0.02}$	$0.24^{+0.04}_{-0.05}$	.....	1.63×10^{-4}	26.4 (23)	1.15	15.3
100219A	4.667	pow	sn	$0.75^{+0.04}_{-0.04}$	$0.16^{+0.05}_{-0.05}$	.....	2.21×10^{-4}	5.9 (9)	0.66	11.4
111008A	4.990	bknpow	sn	$0.38^{+0.21}_{-0.02}$	$0.18^{+0.05}_{-0.15}$	9.96×10^{-3}	9.47×10^{-3}	28.1 (19)	1.48	6.8
140428A	4.680	bknpow	sn	$0.74^{+0.15}_{-0.24}$	$0.15^{+0.13}_{-0.11}$	2.36×10^{-1}	2.36×10^{-3}	5.8 (5)	1.16	2.6
140614A	4.233	bknpow	sn	$0.32^{+0.31}_{-0.32}$	$0.27^{+0.09}_{-0.19}$	9.94×10^{-3}	2.89×10^{-3}	5.6 (8)	0.70	4.1
151027B	4.062	bknpow	sn	$0.51^{+0.07}_{-0.02}$	$0.09^{+0.03}_{-0.05}$	9.93×10^{-3}	3.31×10^{-3}	16.8 (16)	1.05	8.8
151112A	4.270	bknpow	sn	$0.71^{+0.06}_{-0.07}$	$0.41^{+0.11}_{-0.12}$	$1.35 \times 10^{+0}$	2.59×10^{-4}	23.0 (25)	0.92	11.4

Notes. In the top section of the table we list the best-fit parameters from fitting the local extinction curves. In case we found evidence for a medium amount of dust ($A_V > 0.1$ mag), we also fitted the SN extinction curve, for which the corresponding best-fit parameters are listed at the bottom part of the table. [(a)] Spectral slope in the NIR/optical wavelength regime. In case the SED is best-fit with a broken power law (bknpow) the slope in the X-ray is fixed to $\beta_x = \beta_o + 0.5$, otherwise (pow) $\beta_x = \beta_o$ (see Sect. 3.6) [(b)] The common reference time where the broadband SED was created – in hours after the prompt trigger. [(c)] Fit not performed with GROND data (see Sect. 3.7). [(d)] The extinction curve can basically not be identified since there is no evidence for extinction or the A_V is consistent with zero. However, we list the model resulting in the lowest χ^2_{red}.

the GRB lines of sight. Since all of the bursts, including the above-mentioned cases of GRB 071025A and 140428A, can be modeled with locally measured extinction curves, we cannot draw any firm conclusion about whether an SN-type dust extinction curve is truly required for some of the GRBs. Other SN-dominated extinction curves have been proposed by, for example, Bianchi & Schneider (2007), Hirashita et al. (2008, 2010), and Nozawa et al. (2015). But, since only the extinction curve from Todini & Ferrara (2001) and Maiolino et al. (2004) was available for us in an analytical form, we restricted our analysis to their results. A common feature, however, that these extinction curves share is a strong steepening in the UV. This steepening is hard to measure at $z > 4$ anyway because of the dominant absorption from the Lyman-α forest. Also, the low A_V values

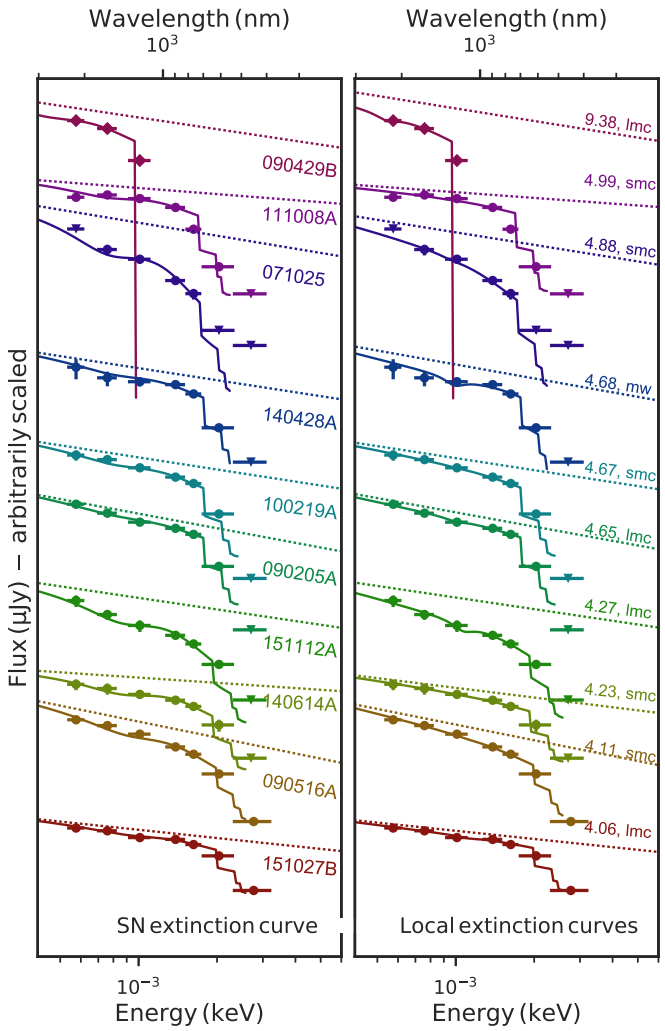

Fig. 8. Similar to Fig. 7, but zoomed into the optical and NIR regime (the full plot is displayed in Fig. C.1). In the left inset we show the SEDs for the 10 GRBs that show evidence for a medium amount of dust ($A_V > 0.1$ mag) fitted with the SN extinction curve. For comparison, in the right inset we show again the best result when performing the fit with local extinction curves. The goodness of fit is comparable in both scenarios (see Table 2 and Sect. 4).

combined with a limited wavelength coverage limit the distinction of the various characteristic features. So from here, we focus the discussion to the somewhat unexpected lack of highly dust-extinguished GRBs, which can only be explained as a result of one or both of the following suppositions:

1. At a redshift of $z > 4$, when the Universe was less than ~1.6 Gyr old, not enough dust was present in young GRB host galaxies to cause visual extinctions of $A_V > 0.5$ mag.
2. High dust-extinguished GRBs at $z > 4$ are absent in our sample and other samples because their optical and NIR afterglow was too faint to be detected.

In order to check if the lack of higher extinguished afterglows can be explained with an observational bias, we calculated theoretical GROND detection thresholds for three of the afterglow SEDs from Table 2, by artificially placing them at redshifts between $0 < z < 10$. The SED for GRB 131117A corresponds to an epoch observed at just ~ 0.1 h after the trigger and is additionally very flat ($\beta_o \sim 0.25$). The SED of GRB 140311A is more representative of the GRBs studied here; its SED is much

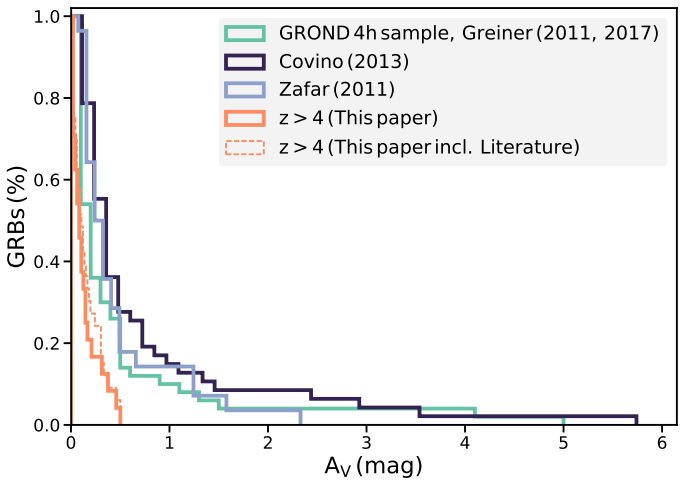

Fig. 9. Normalized and reversed cumulative distribution of the host intrinsic dust extinction derived for the GRBs with redshift $z > 4$ from this work, compared to the BAT6 sample (Covino et al. 2013) and GROND 4h sample (Greiner et al. 2011), which are both unbiased samples. We also plot the data from Zafar et al. (2011a); this plot is based on the GRB sample from Fynbo et al. (2009) and likely biased toward low extinction sightlines.

Table 3. Host intrinsic visual extinction for the GRBs at $z > 4$ that were not observed by GROND.

GRB yymmdd#	Redshift[a] (z)	A_V (mag)	Reference
000131	4.500	$0.29^{+0.18}_{-0.18}$	(1)
050502B	$5.2^{+0.3}_{-0.3}$	<0.5	(2)
050505	4.275	$0.29^{+0.06}_{-0.06}$	(3)
050814	$5.77^{+0.12}_{-0.12}$	$0.23^{+0.15}_{-0.15}$	(1)
050904	6.295	<0.32	(4) (5)
050922B	4.5 ± 0.5	...	...
060206	4.048	<0.17	(6)
060223A	4.406	...	...
060510B	4.941	...	...
060522	5.11	...	...
060927	5.467	<0.12	(7)
100302A	4.813	...	...
120521C	6.0	<0.05	(8)
120923A[b]	7.84	0.06	(9)
140518A	4.707	$0.03^{+0.02}_{-0.02}$	(10)

Notes. All values are collected from the literature. [(a)] Photometric if given with errors, spectroscopic otherwise. [(b)] Observed by GROND but not detected.

References. (1) Curran et al. (2008); (2) Afonso et al. (2011); (3) Hurkett et al. (2006); (4) Zafar et al. (2010); (5) Stratta et al. (2011); (6) Covino et al. (2013); (7) Zafar et al. (2011b); (8) Laskar et al. (2014); (9) Tanvir et al. (2017); (10) Littlejohns et al. (2015).

steeper ($\beta_o \sim 0.85$) and was created from the afterglow emission at $T_0 + 9.8$ h. For both of these bursts we assume a typical limiting magnitude in the GROND z' band of $z'_{lim} = 24.2$ mag. As a more extreme example, we also calculate the detection threshold for the SED of the very high redshift GRB 090423, which corresponds to an observation taken at $T_0 + 17.3$ h ($\beta_o \sim 0.88$). Here we assume a typical GROND H-band limiting magnitude of $H_{lim} = 22$ mag. Our results are represented by the dashed lines in Fig. 10, where we plot our A_V values against redshift in comparison to different GRB samples at mostly lower redshift.

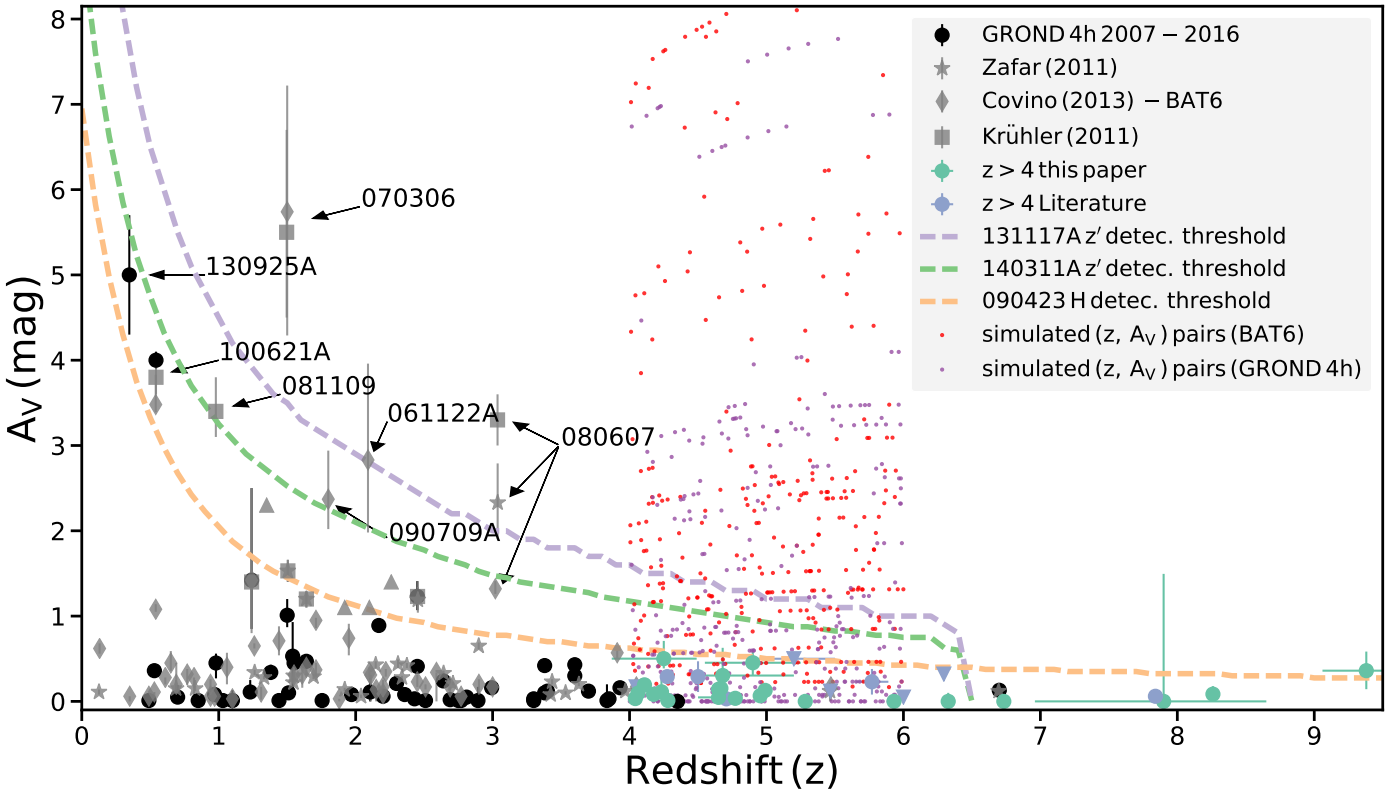

Fig. 10. Host intrinsic visual dust extinction A_V toward the line of sight of the GRB plotted against redshift for the GRBs analyzed in this paper and in comparison to different samples at mostly lower redshift (Covino et al. 2013; Greiner et al. 2011; Krühler et al. 2011a; Zafar et al. 2011a). The dashed lines represent the GROND detection thresholds for GRB 131117, 140311A, and 090423 in the given band (see Sect. 5). Highly extinguished GRBs are labeled. The red and purple dots represent 500 from the 10^6 simulated (z, A_V(obs.)) pairs.

Above these lines, the dust extinction would be so high that these GRBs would not have been detected by GROND (at the given time the SED was created and if the GRB had been detected from the redshift we artificially placed it at). One can see that a few exceptions fall above these lines. For example, GRB 070306 was observed with a larger telescope and GRB 080607, 061222A, and 090709A were observed within a very short time after the *Swift*/BAT trigger (Cenko & Fox 2006; Jaunsen et al. 2008; Cenko et al. 2010a; Perley et al. 2011).

Although the detection thresholds for these burst clearly show that it is much harder to detect highly extinguished afterglows at $z > 4$, the absence of burst with $0.5 < A_V < 1.5$ mag, i.e., the lack of data points between these lines given the size of our sample, seems somewhat unexpected. Therefore, to further test to what extent we suffer from an observational bias, we made the following Monte Carlo simulation. We derived the intrinsic brightness in the GROND z' band for the 17 GRBs at redshift $4.0 < z < 6.0$ and distributed random values out of the A_V distribution from the GROND 4h sample (Greiner et al. 2011) or the BAT 6 sample (Covino et al. 2013), by also putting each GRB at a random redshift between $4.0 < z < 6.0$[6]. We thus assume that the intrinsic brightness of the GRB is unrelated to the absorption by dust within the host galaxy. In Fig. 10 we plot 500 from 10^6 simulated (z, A_V(obs.)) pairs for both samples. In case of the A_V distribution from (Greiner et al. 2011), on average we would expect to find $n = 0.8 \pm 0.9$ bursts with $A_V > 0.5$ mag that are brighter than 24.2 mag in the z' band and $n = 2.0 \pm 1.3$ in case of the A_V distribution from the BAT 6 sample. The probabilities of detecting zero GRBs with $A_V > 0.5$ mag are $p = 43.6\%$ and $p = 11.4\%$, respectively. To detect at least one burst with $A_V > 0.5$ mag at a confidence of 1σ, it would require a sample size of $n = 21$ (GROND 4h sample) or $n = 10$ (BAT 6) GRBs. The different outcomes of the two samples can be explained by the higher percentage of bursts with $0.5 < A_V \lesssim 2.0$ mag in the sample from Covino et al. (2013), which are the only bursts we are theoretically able to detect at $z > 4$, given our brightness distribution. Although the case is less clear for the A_V distribution from the GROND 4h sample, our sample size should be big enough to contain at least one GRB with $A_V > 0.5$ mag at least after also including the GRBs that were not observed with GROND.

Hence, these considerations suggest that we partly suffer from an observational bias toward highly extinguished GRBs, meaning that we cannot expect to easily detect bursts with $A_V > 0.5$ mag at $z > 4$ with a sensitivity of about ~24 mag (reachable with a 2m telescope). Nevertheless, our results can be interpreted as evidence that GRB host galaxies at high redshift are on average less dusty than at $z \sim 2$.

To further test the occurrence of $A_V > 0.5$ mag at $z > 4$, very rapid observations at NIR wavelengths are required, which are difficult to achieve in large numbers from Chile since the South Atlantic Anomaly suppresses the number of night-time GRBs by more than a factor of two.

Acknowledgements. The author acknowledges support from a studentship at the European Southern Observatory in Chile and thanks the many astronomers who dedicated their time observing the numerous GRBs during the operation of GROND between 2007 and 2016. We also thank the anonymous referee for providing valuable and constructive feedback that help improving the presentation

[6] Since the extinction from dust increases from the red to blue wavelengths, this of course increases the extinction in the given (observer frame) band.

of this work. J.B. and T.K. acknowledge support through the Sofja Kovalevskaja Award to P.S. from the Alexander von Humboldt Foundation of Germany. Part of the funding for GROND (both hardware and personnel) was generously granted from the Leibniz-Prize to Prof. G. Hasinger (DFG grant HA 1850/28-1).

References

Aceituno, F. J., Castro-Tirado, A. J., Sanchez-Ramirez, R., & Gorosabel, J. 2014, GRB Coordinates Network, 16182
Afonso, P., Greiner, J., Pian, E., et al. 2011, A&A, 526, A154
Andersen, M. I., Hjorth, J., Pedersen, H., et al. 2000, A&A, 364, L54
Barthelmy, S. D., Baumgartner, W. H., Cummings, J. R., et al. 2010, GRB Coordinates Network, 11218
Berger, E., Penprase, B. E., Cenko, S. B., et al. 2006, ApJ, 642, 979
Bianchi, S., & Schneider, R. 2007, MNRAS, 378, 973
Bolmer, J., Knust, F., & Greiner, J. 2015, GRB Coordinates Network, 18603
Buchner, J., Schulze, S., & Bauer, F. E. 2017, MNRAS, 464, 4545
Butler, N., Watson, A. M., Kutyrev, A., et al. 2014, GRB Coordinates Network, 15928
Campana, S., Salvaterra, R., Ferrara, A., & Pallottini, A. 2015, A&A, 575, A43
Cardelli, J. A., Clayton, G. C., & Mathis, J. S. 1989, ApJ, 345, 245
Castro-Tirado, A. J., Sánchez-Ramírez, R., Ellison, S. L., et al. 2013, ArXiv e-prints [arXiv:1312.5631], unpublished
Cenko, S. B., & Fox, D. B. 2006, GRB Coordinates Network, 5978
Cenko, S. B., Berger, E., Djorgovski, S. G., Mahabal, A. A., & Fox, D. B. 2006, GRB Coordinates Network, 5155
Cenko, S. B., Kelemen, J., Harrison, F. A., et al. 2009, ApJ, 693, 1484
Cenko, S. B., Butler, N. R., Ofek, E. O., et al. 2010a, AJ, 140, 224
Cenko, S. B., Perley, D. A., Morgan, A. N., et al. 2010b, GRB Coordinates Network, 10752
Chary, R., Berger, E., & Cowie, L. 2007, ApJ, 671, 272
Chornock, R., Cucchiara, A., Fox, D., & Berger, E. 2010, GRB Coordinates Network, 10466
Chornock, R., Berger, E., Fox, D. B., et al. 2014, ArXiv e-prints [arXiv:1405.7400]
Covino, S., Melandri, A., Salvaterra, R., et al. 2013, MNRAS, 432, 1231
Cucchiara, A., & Cenko, S. B. 2013, GRB Coordinates Network, 15624
Cucchiara, A., Levan, A. J., Fox, D. B., et al. 2011, ApJ, 736, 7
Curran, P. A., Wijers, R. A. M. J., Heemskerk, M. H. M., et al. 2008, A&A, 490, 1047
D'Avanzo, P., Perri, M., Fugazza, D., et al. 2010, A&A, 522, A20
D'Avanzo, P., Bernardini, M. G., D'Elia, V., et al. 2014, GRB Coordinates Network, 16267
De Cia, A., Ledoux, C., Savaglio, S., Schady, P., & Vreeswijk, P. M. 2013, A&A, 560, A88
De Looze, I., Barlow, M. J., Swinyard, B. M., et al. 2017, MNRAS, 465, 3309
de Ugarte Postigo, A., Gorosabel, J., Malesani, D., Fynbo, J. P. U., & Levan, A. J. 2009, GRB Coordinates Network, 9381
de Ugarte Postigo, A., Gorosabel, J., Xu, D., et al. 2014, GRB Coordinates Network, 15921
Evangelista, Y., Soffitta, P., Del Monte, E., et al. 2008, GRB Coordinates Network, 8133
Evans, P. A., Beardmore, A. P., Page, K. L., et al. 2009, MNRAS, 397, 1177
Fitzpatrick, E. L., & Massa, D. 1986, ApJ, 307, 286
Fugazza, D., Thoene, C. C., D'Elia, V., et al. 2009, GRB Coordinates Network, 8892
Fynbo, J. P. U., Starling, R. L. C., Ledoux, C., et al. 2006, A&A, 451, L47
Fynbo, J. P. U., Jakobsson, P., Prochaska, J. X., et al. 2009, ApJS, 185, 526
Fynbo, J. P. U., Krühler, T., Leighly, K., et al. 2014, A&A, 572, A12
Galama, T. J., & Wijers, R. A. M. J. 2001, ApJ, 549, L209
Gehrels, N., Ramirez-Ruiz, E., & Fox, D. B. 2009, ARA&A, 47, 567
Goldstein, A., & van der Horst, A. 2008, GRB Coordinates Network, 8245
Gomez, H. L., Krause, O., Barlow, M. J., et al. 2012, ApJ, 760, 96
Gorosabel, J., de Ugarte Postigo, A., Montes, D., Klutsch, A., & Castro-Tirado, A. J. 2009, GRB Coordinates Network, 9379
Greiner, J., Clemens, C., Krühler, T., et al. 2009a, A&A, 498, 89
Greiner, J., Krühler, T., Fynbo, J. P. U., et al. 2009b, ApJ, 693, 1610
Greiner, J., Krühler, T., McBreen, S., et al. 2009c, ApJ, 693, 1912
Greiner, J., Krühler, T., Klose, S., et al. 2011, A&A, 526, A30
Greiner, J., Fox, D. B., Schady, P., et al. 2015, ApJ, 809, 76
Hartoog, O. E., Malesani, D., Fynbo, J. P. U., et al. 2015, A&A, 580, A139
Hartoog, O. E., Xu, D., Malesani, D., et al. 2013, GRB Coordinates Network, 15494
Hirashita, H., Nozawa, T., Takeuchi, T. T., & Kozasa, T. 2008, MNRAS, 384, 1725
Hirashita, H., Nozawa, T., Yan, H., & Kozasa, T. 2010, MNRAS, 404, 1437
Hirashita, H., Ferrara, A., Dayal, P., & Ouchi, M. 2014, MNRAS, 443, 1704
Hjorth, J., Malesani, D., Jakobsson, P., et al. 2012, ApJ, 756, 187
Hjorth, J., Vreeswijk, P. M., Gall, C., & Watson, D. 2013, ApJ, 768, 173
Hunt, L. K., Palazzi, E., Michałowski, M. J., et al. 2014, A&A, 565, A112
Hurkett, C. P., Osborne, J. P., Page, K. L., et al. 2006, MNRAS, 368, 1101
Im, M., Choi, C., Jun, H., et al. 2010, GRB Coordinates Network, 11222
Indebetouw, R., Matsuura, M., Dwek, E., et al. 2014, ApJ, 782, L2
Jang, M., Im, M., Lee, I., et al. 2011, ApJ, 741, L20
Jaunsen, A. O., Rol, E., Watson, D. J., et al. 2008, ApJ, 681, 453
Jeong, S., Sanchez-Ramirez, R., Gorosabel, J., & Castro-Tirado, A. J. 2014, GRB Coordinates Network, 15936
Kalberla, P. M. W., Burton, W. B., Hartmann, D., et al. 2005, A&A, 440, 775
Kann, D. A., Klose, S., & Zeh, A. 2006, ApJ, 641, 993
Kann, D. A., Nicuesa Guelbenzu, A., & Greiner, J. 2013, GRB Coordinates Network, 15632
Kawai, N., Kosugi, G., Aoki, K., et al. 2006, Nature, 440, 184
Kocevski, D., Barthelmy, S. D., Lien, A. Y., et al. 2014, GRB Coordinates Network, 16177
Krimm, H. A., Beardmore, A. P., Evans, P. A., et al. 2009, GRB Coordinates Network, 9198
Krühler, T., Küpcü Yoldaş, A., Greiner, J., et al. 2008, ApJ, 685, 376
Krühler, T., Greiner, J., Schady, P., et al. 2011a, A&A, 534, A108
Krühler, T., Schady, P., Greiner, J., et al. 2011b, A&A, 526, A153
Krühler, T., Ledoux, C., Fynbo, J. P. U., et al. 2013, A&A, 557, A18
Krühler, T., Vreeswijk, P. M., & Fynbo, J. P. U. 2014, GRB Coordinates Network, 16401
Kumar, P., & Zhang, B. 2015, Phys. Rep., 561, 1
Laporte, N., Ellis, R. S., Boone, F., et al. 2017, ApJ, 837, L21
Laskar, T., Berger, E., Tanvir, N., et al. 2014, ApJ, 781, 1
Ledoux, C., Vreeswijk, P. M., Smette, A., et al. 2009, A&A, 506, 661
Littlejohns, O. M., Tanvir, N. R., Willingale, R., et al. 2013, MNRAS, 436, 3640
Littlejohns, O. M., Butler, N. R., Cucchiara, A., et al. 2015, MNRAS, 449, 2919
Maiolino, R., Schneider, R., Oliva, E., et al. 2004, Nature, 431, 533
Malesani, D., Barthelmy, S. D., Evans, P. A., et al. 2015a, GRB Coordinates Network, 18588
Malesani, D., Tanvir, N. R., Xu, D., et al. 2015b, GRB Coordinates Network, 18501
Mancini, M., Schneider, R., Graziani, L., et al. 2015, MNRAS, 451, L70
Mao, J., Malesani, D., D'Avanzo, P., et al. 2012, A&A, 538, A1
Margutti, R., Berger, E., Chornock, R., et al. 2014, GRB Coordinates Network, 16338
Marshall, F. E., Barthelmy, S. D., Beardmore, A. P., et al. 2010, GRB Coordinates Network, 11214
Matsuura, M., Dwek, E., Barlow, M. J., et al. 2015, ApJ, 800, 50
McGuire, J. T. W., Tanvir, N. R., Levan, A. J., et al. 2016, ApJ, 825, 135
Melandri, A., Bernardini, M. G., D'Avanzo, P., et al. 2015, A&A, 581, A86
Mereghetti, S., Paizis, A., Gotz, D., et al. 2010, GRB Coordinates Network, 10772
Michałowski, M. J. 2015, A&A, 577, A80
Morgan, A. N., Perley, D. A., Klein, C. R., & Bloom, J. S. 2010, GRB Coordinates Network, 10747
Nozawa, T., Kozasa, T., Habe, A., et al. 2007, ApJ, 666, 955
Nozawa, T., Kozasa, T., & Nomoto, K. 2012, ApJ, 756, L35
Nozawa, T., Asano, R. S., Hirashita, H., & Takeuchi, T. T. 2015, MNRAS, 447, L16
Pagani, C., Baumgartner, W. H., Burrows, D. N., et al. 2007, GRB Coordinates Network, 6986
Page, M. J., Breeveld, A. A., Burrows, D. N., et al. 2012, GRB Coordinates Network, 13454
Page, M. J., Barthelmy, S. D., Burrows, D. N., et al. 2013, GRB Coordinates Network, 15490
Page, K. L., Barthelmy, S. D., Burrows, D. N., et al. 2014, GRB Coordinates Network, 16391
Patel, M., Warren, S. J., Mortlock, D. J., & Fynbo, J. P. U. 2010, A&A, 512, L3
Perley, D. A. 2014a, GRB Coordinates Network, 16180
Perley, D. A. 2014b, GRB Coordinates Network, 16181
Perley, D. A., Bloom, J. S., Butler, N. R., et al. 2008, ApJ, 672, 449
Perley, D. A., Bloom, J. S., Klein, C. R., et al. 2010, MNRAS, 406, 2473
Perley, D. A., Morgan, A. N., Updike, A., et al. 2011, AJ, 141, 36
Perley, D. A., Levan, A. J., Tanvir, N. R., et al. 2013, ApJ, 778, 128
Perley, D. A., Krühler, T., Schulze, S., et al. 2016a, ApJ, 817, 7
Perley, D. A., Tanvir, N. R., Hjorth, J., et al. 2016b, ApJ, 817, 8
Perri, M., Barthelmy, S. D., Baumgartner, W. H., et al. 2009, GRB Coordinates Network, 8884
Price, P. A., Songaila, A., Cowie, L. L., et al. 2007, ApJ, 663, L57
Racusin, J. L., Baumgartner, W. H., Gehrels, N., et al. 2014, GRB Coordinates Network, 15944

Rossi, A., Klose, S., Ferrero, P., et al. 2012, A&A, 545, A77
Rowlinson, B. A., Beardmore, A. P., Evans, P. A., et al. 2009, GRB Coordinates Network, 9374
Rowlinson, A., Barthelmy, S. D., Baumgartner, W. H., et al. 2010, GRB Coordinates Network, 10430
Ruiz-Velasco, A. E., Swan, H., Troja, E., et al. 2007, ApJ, 669, 1
Salvaterra, R., Della Valle, M., Campana, S., et al. 2009, Nature, 461, 1258
Salvaterra, R., Campana, S., Vergani, S. D., et al. 2012, ApJ, 749, 68
Sarangi, A., & Cherchneff, I. 2013, ApJ, 776, 107
Savaglio, S., & Fall, S. M. 2004, ApJ, 614, 293
Saxton, C. J., Barthelmy, S. D., Beardmore, A. P., et al. 2011, GRB Coordinates Network, 12423
Schlafly, E. F., & Finkbeiner, D. P. 2011, ApJ, 737, 103
Schady, P., Mason, K. O., Page, M. J., et al. 2007, MNRAS, 377, 273
Schady, P., Beardmore, A. P., Cummings, J. R., et al. 2008, GRB Coordinates Network, 8217
Schady, P., Dwelly, T., Page, M. J., et al. 2012, A&A, 537, A15
Schneider, R., Omukai, K., Bianchi, S., & Valiante, R. 2012a, MNRAS, 419, 1566
Schneider, R., Omukai, K., Limongi, M., et al. 2012b, MNRAS, 423, L60
Schulze, S., Chapman, R., Hjorth, J., et al. 2015, ApJ, 808, 73
Siegel, M. H., & Marshall, F. E. 2010, GRB Coordinates Network, 11237
Silvia, D. W., Smith, B. D., & Shull, J. M. 2012, ApJ, 748, 12
Skrutskie, M. F., Cutri, R. M., Stiening, R., et al. 2006, AJ, 131, 1163
Sparre, M., Hartoog, O. E., Krühler, T., et al. 2014, ApJ, 785, 150
Starling, R. L. C., Willingale, R., Tanvir, N. R., et al. 2013, MNRAS, 431, 3159
Stratta, G., Maiolino, R., Fiore, F., & D'Elia, V. 2007, ApJ, 661, L9
Stratta, G., Gallerani, S., & Maiolino, R. 2011, A&A, 532, A45
Tanvir, N. R., Fox, D. B., Levan, A. J., et al. 2009, Nature, 461, 1254
Tanvir, N. R., Levan, A. J., Fruchter, A. S., et al. 2012, ApJ, 754, 46
Tanvir, N. R., Levan, A. J., Wiersema, K., & Cucchiara, A. 2014, GRB Coordinates Network, 15961
Tanvir, N. R., Laskar, T., Levan, A. J., et al. 2017, ArXiv e-prints [arXiv:1703.09052]
Thoene, C. C., de Ugarte Postigo, A., & Ricci, D. 2008, GRB Coordinates Network, 8135
Thöne, C. C., Fynbo, J. P. U., Goldoni, P., et al. 2013, MNRAS, 428, 3590
Todini, P., & Ferrara, A. 2001, MNRAS, 325, 726
Tody, D. 1993, in Astronomical Data Analysis Software and Systems II, eds. R. J. Hanisch, R. J. V. Brissenden, & J. Barnes, ASP conf. Ser., 52, 173
Ukwatta, T. N., Barthelmy, S. D., Baumgartner, W. H., et al. 2015, GRB Coordinates Network, 18499
Ukwatta, T. N., Barthelmy, S. D., Evans, P. A., et al. 2009, GRB Coordinates Network, 9281
Ukwatta, T. N., Barthelmy, S. D., Gehrels, N., et al. 2013, GRB Coordinates Network, 14781
Valiante, R., Schneider, R., Bianchi, S., & Andersen, A. C. 2009, MNRAS, 397, 1661
Volnova, A., Pozanenko, A., Korobtsev, I., Klunko, E., & Eselevich, M. 2014a, GRB Coordinates Network, 15917
Volnova, A., Tungalag, N., Schmalz, S., et al. 2014b, GRB Coordinates Network, 15918
Watson, A. M., Butler, N., Kutyrev, A., et al. 2015a, GRB Coordinates Network, 18512
Watson, D., Christensen, L., Knudsen, K. K., et al. 2015b, Nature, 519, 327
Wiersema, K., Flores, H., D'Elia, V., et al. 2011, GRB Coordinates Network, 12431
Wiseman, P., Schady, P., Bolmer, J., et al. 2017, A&A, 599, A24
Xu, D., Fynbo, J. P. U., D'Elia, V., & Tanvir, N. R. 2012, GRB Coordinates Network, 13460
Xu, D., Malesani, D., Schulze, S., et al. 2013, GRB Coordinates Network, 14816
Xu, D., Bai, C.-H., Zhang, X., Esamdin, A., & Ma, L. 2014a, GRB Coordinates Network, 15956
Xu, D., Niu, H.-B., Feng, G.-J., et al. 2014b, GRB Coordinates Network, 15916
Xu, D., Tanvir, N. R., Malesani, D., & Fynbo, J. P. U. 2015, GRB Coordinates Network, 18506
Yershov, V. N., Barthelmy, S. D., Krimm, H. A., et al. 2012, GRB Coordinates Network, 13796
Zafar, T., Watson, D. J., Malesani, D., et al. 2010, A&A, 515, A94
Zafar, T., Watson, D., Fynbo, J. P. U., et al. 2011a, A&A, 532, A143
Zafar, T., Watson, D. J., Tanvir, N. R., et al. 2011b, ApJ, 735, 2
Zafar, T., Watson, D., Elíasdóttir, Á., et al. 2012, ApJ, 753, 82
Zaninoni, E., Bernardini, M. G., Margutti, R., Oates, S., & Chincarini, G. 2013, A&A, 557, A12

Appendix A: Photometric redshifts

In Fig. A.1 to Fig. A.5 we show the GROND SEDs and A_V versus redshift contour plots for GRB 071025, 080916C, 100518A, 140428A, and 151112A.

Individual bursts

GRB 071025. Is best fit with the SN-like dust extinction law, $A_V = 0.39^{+0.20}_{-0.14}$ mag, and a photometric redshift of $z_{\rm phot} = 4.88 \pm 0.35$, which is consistent with the photometric redshifts of $4.4 < z_{\rm phot} < 5.2$ and $4.6 < z_{\rm phot} < 4.85^{+0.05}_{-0.10}$ reported by Perley et al. (2010) and Jang et al. (2011), who also find evidence for extinction caused by SN-synthesized dust. We limited the redshift parameter space to $z > 2$ to prevent a low-redshift solution that would be in strong disagreement with the results from the above-mentioned authors.

GRB 080916C. Is best fit with $z_{\rm phot} = 4.28^{+0.06}_{-0.10}$, $A_V = 0.11^{+0.08}_{-0.09}$ mag and the SMC extinction curve. This is consistent with the results from Greiner et al. (2009a).

GRB 100518A. For GRB 100518A we cannot confirm the previously reported redshift of $z_{\rm phot} = 4.0^{+0.3}_{-0.5}$ (Greiner et al. 2015). Our GROND magnitudes, as listed in Table D.1, are best fit with a $z_{\rm phot} = 3.50^{+0.50}_{-0.62}$ and a host intrinsic extinction of $A_V = 0.19^{+1.48}_{-0.19}$ mag, indicating that it is difficult to distinguish between a high redshift and low visual extinction or vice versa. The high redshift ($z \gtrsim 3$) nature of the GRB is further supported from late-time observations in the *VLT*/FORS2 *R* band, not revealing a host galaxy down to a limit of >28.7 mag (Greiner et al. 2015).

GRB 140428A. Is best fit with a photometric redshift of $z_{\rm phot} = 4.68^{+0.52}_{-0.18}$, which is in accordance with the estimate of $z \sim 4.7$ from the LRIS spectrum (Perley 2014b) and the SN extinction law ($A_V = 0.36^{+0.06}_{-0.32}$ mag).

GRB 151112A. Is best fit with a photometric redshift of $z_{\rm phot} = 4.27^{+0.24}_{-0.38}$ and the SMC extinction law ($A_V = 0.08^{+0.34}_{-0.02}$ mag). This is consistent with the initial estimate from Bolmer et al. (2015).

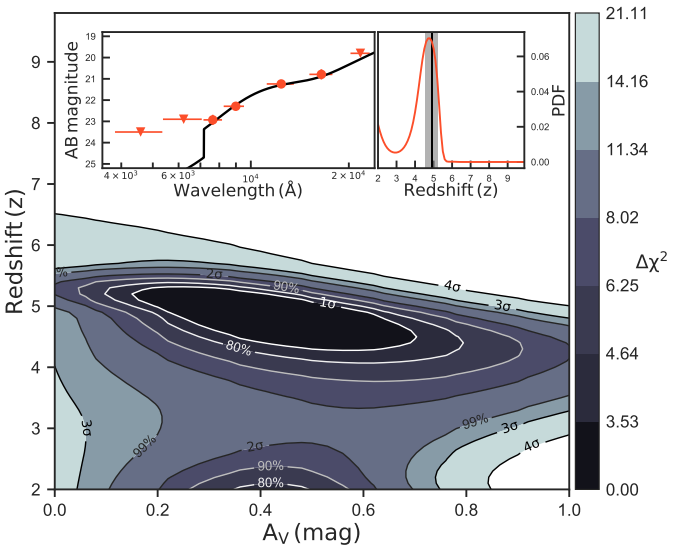

Fig. A.1. GRB 071025.

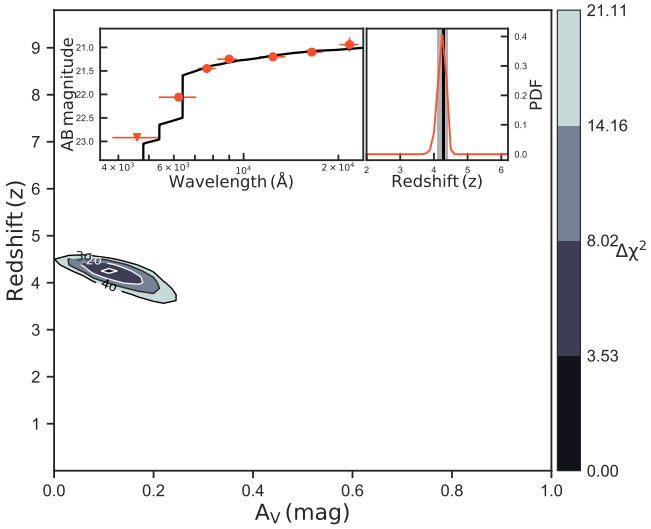

Fig. A.2. GRB 080916C.

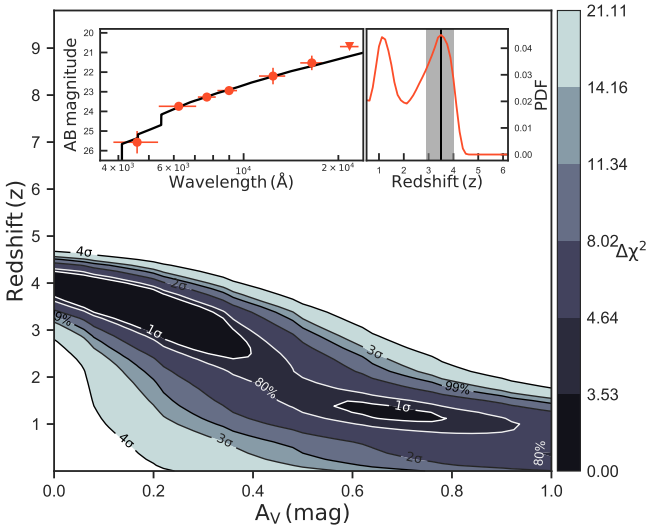

Fig. A.3. GRB 100518A.

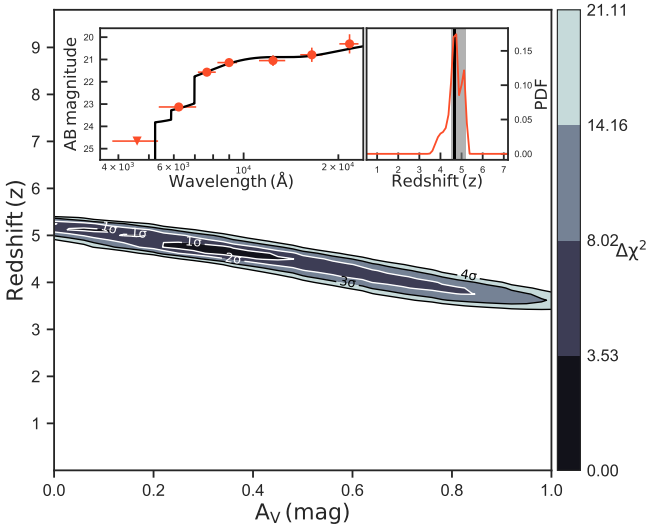

Fig. A.4. GRB 140428A.

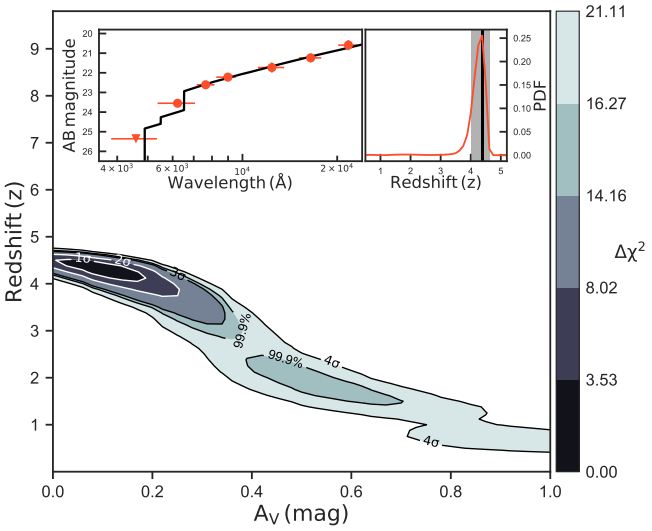

Fig. A.5. GRB 151112A.

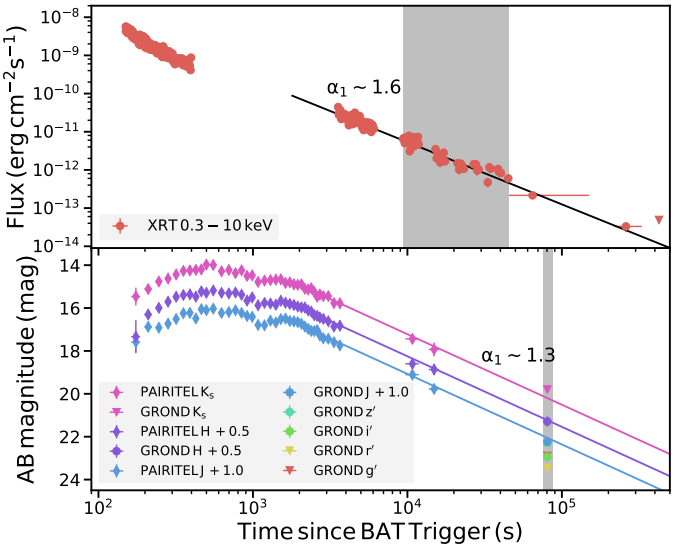

Fig. B.1. GRB 071025.

Appendix B: Light curves of the X-ray, optical, and near-infrared afterglow

The GROND and XRT observations of the afterglow were supplemented – if available – by additional observations reported in the literature to create and fit as well-covered light curves as possible. To fit the afterglow light curves we used phenomenological models such as a single or smoothly broken power law or a combination of both (similar to, e.g., Zaninoni et al. 2013). Flares and re-brightenings were modeled by adding a Gaussian component, and a possible contribution from the host galaxy was modeled by adding a constant term,

$$F_\nu(t) \propto t^{-\alpha_1}\left(+\left(\left(\frac{t}{t_b}\right)^{-s\cdot\alpha_2}+\left(\frac{t}{t_b}\right)^{-s\cdot\alpha_3}\right)^{-1/s}\right)\left(+e^{-\frac{1}{2}\cdot\left(\frac{t-t_{\rm mid}}{\sigma_t}\right)^2}\right)(+h)\,. \tag{B.1}$$

This method is sufficient to identify regions of temporal (and possibly spectral) evolution and to rescale XRT and/or GROND data to a common reference time. In most cases we kept the GROND data fixed and used the usually better covered XRT light curve to rescale the X-ray spectrum. We only used the model best fit to the GROND light curves for GRB 080825B, for which the XRT light curve consists of only four data points.

All the light curves and best-fit models are shown in Fig. B.1 to Fig. B.21. In each case, the gray shaded areas indicate the time intervals, which were chosen to create the quasi-simultaneous X-ray to NIR broadband SEDs. Additionally, the best-fit models and parameters as well as the references for the data collected from the literature are given in Table C.1.

Finally, for some of the GRBs, the GROND data are already published in various papers (GRB 080913 in Greiner et al. (2009b), GRB 080916C in Greiner et al. (2009a), 090423 in Tanvir et al. (2009), GRB 090429B in Cucchiara et al. (2011), and GRB 100219A in Thöne et al. (2013)). However, because of to improvements of the GROND data reduction pipeline and for reasons of consistency, we decided to re-analyze the data. The complete set of GROND magnitudes is given in Table D.1.

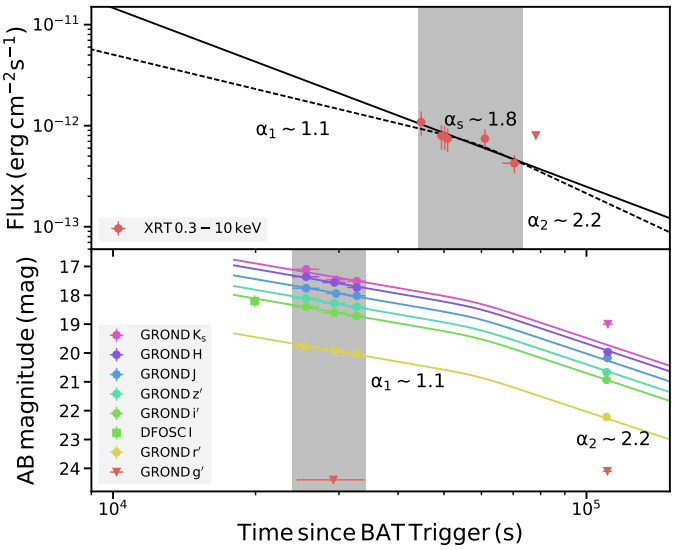

Fig. B.2. GRB 080825B.

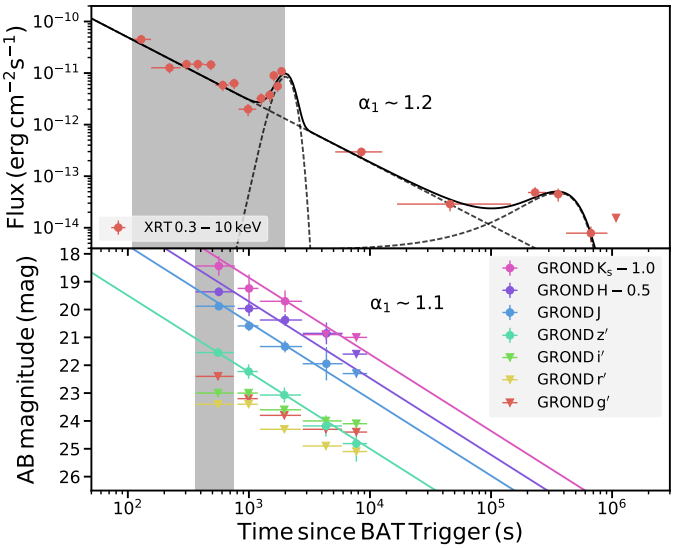

Fig. B.3. GRB 080913.

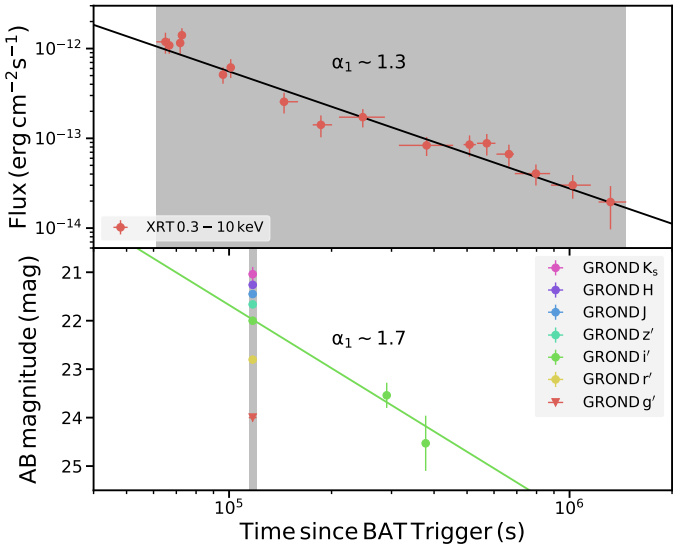

Fig. B.4. GRB 080916C.

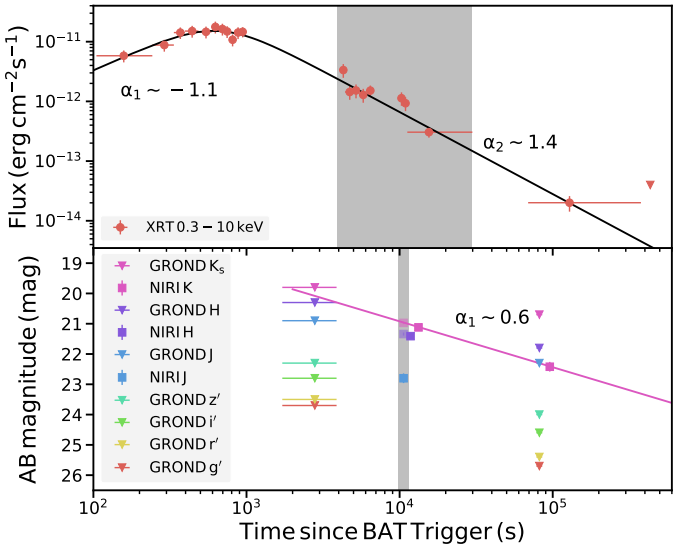

Fig. B.7. GRB 090429B.

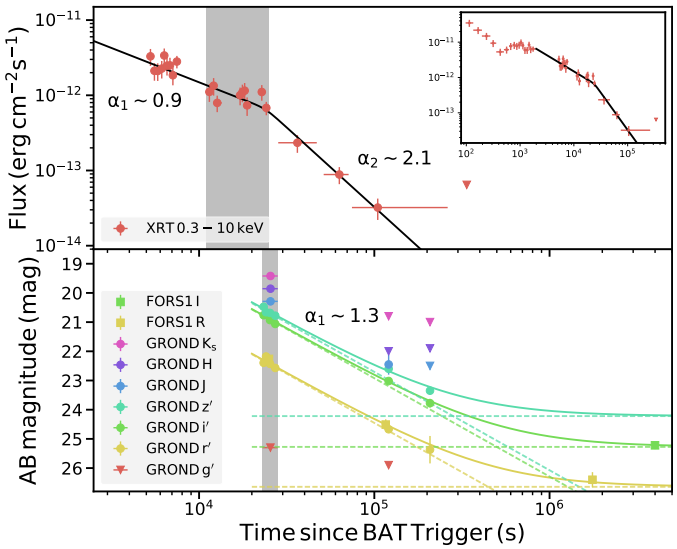

Fig. B.5. GRB 090205.

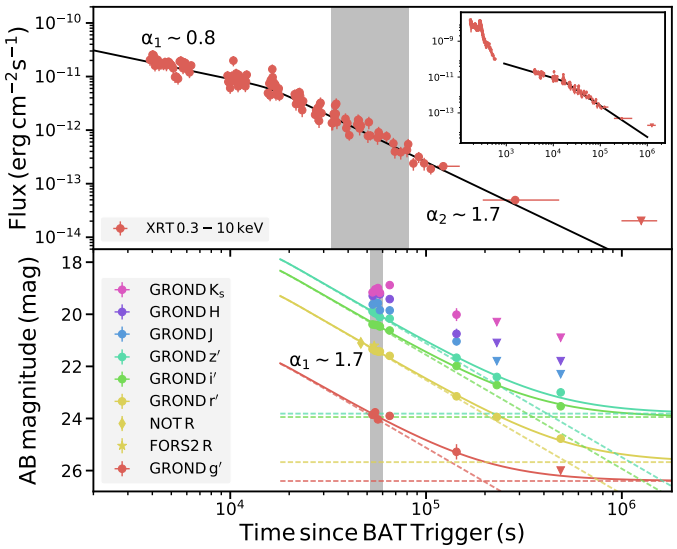

Fig. B.8. GRB 090516A.

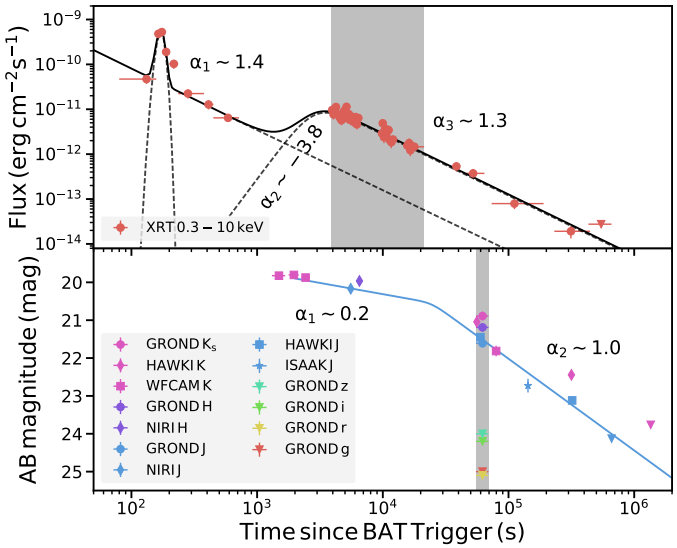

Fig. B.6. GRB 090423.

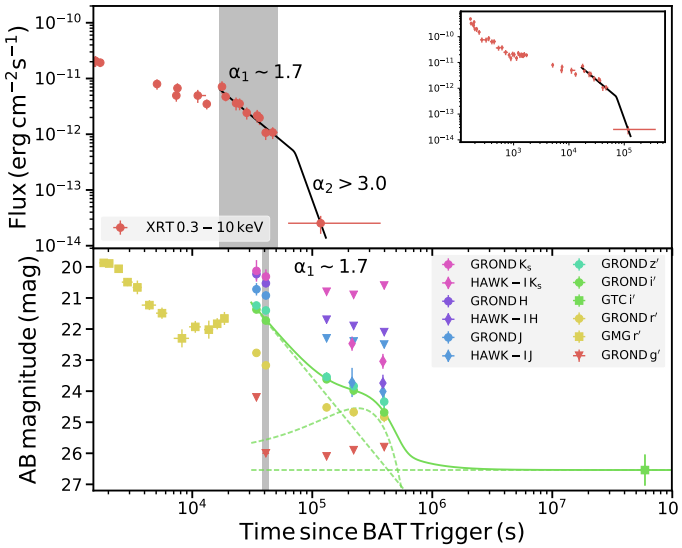

Fig. B.9. GRB 100219A.

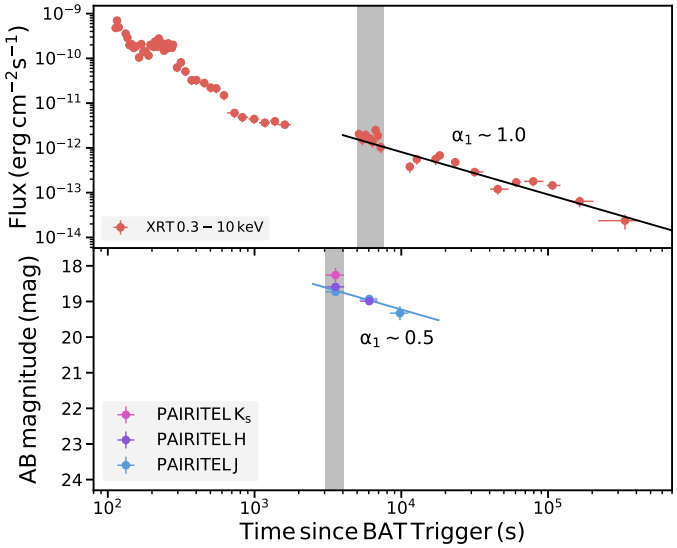

Fig. B.10. GRB 100513A.

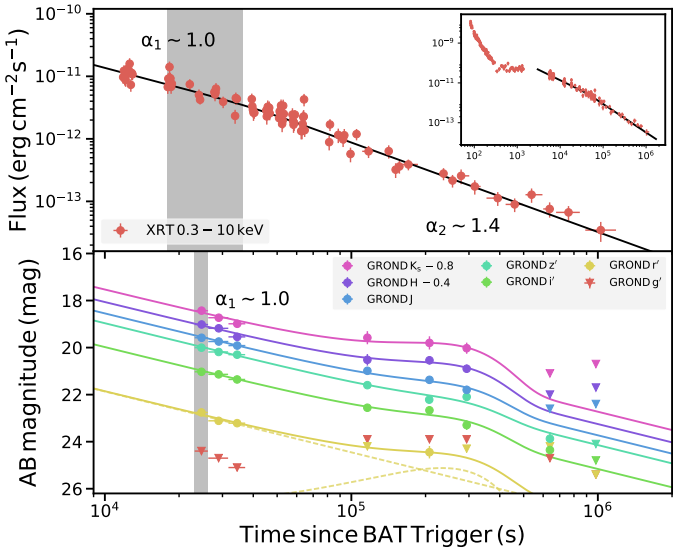

Fig. B.11. GRB 111008A

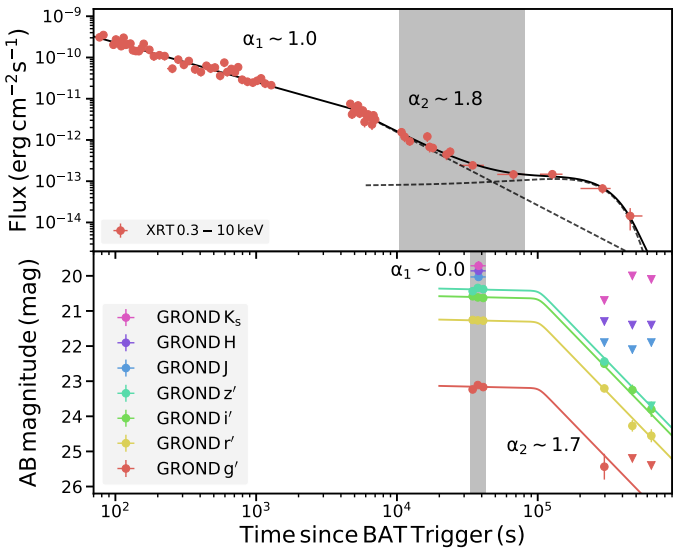

Fig. B.12. GRB 120712A.

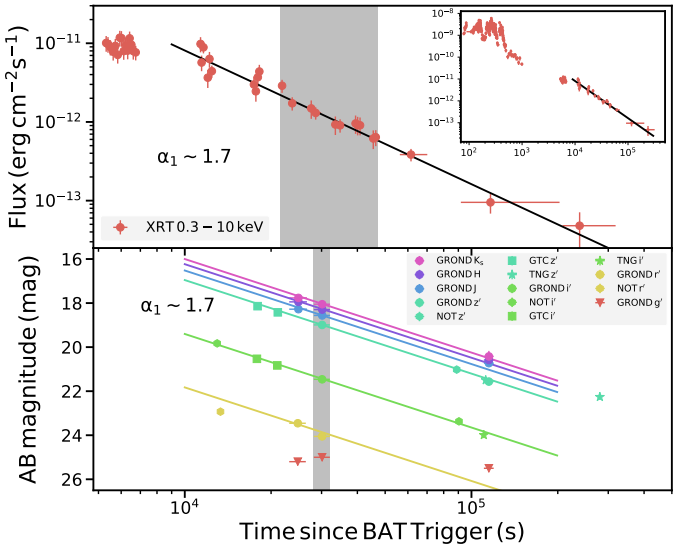

Fig. B.13. GRB 130606A.

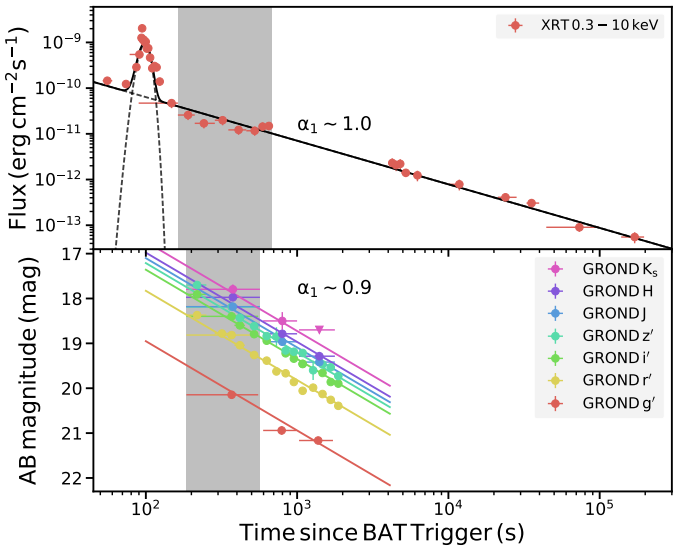

Fig. B.14. GRB 131117A.

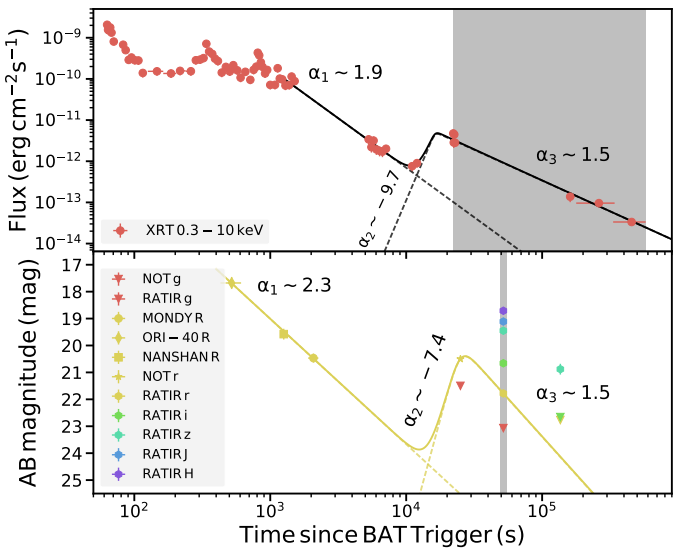

Fig. B.15. GRB 140304A

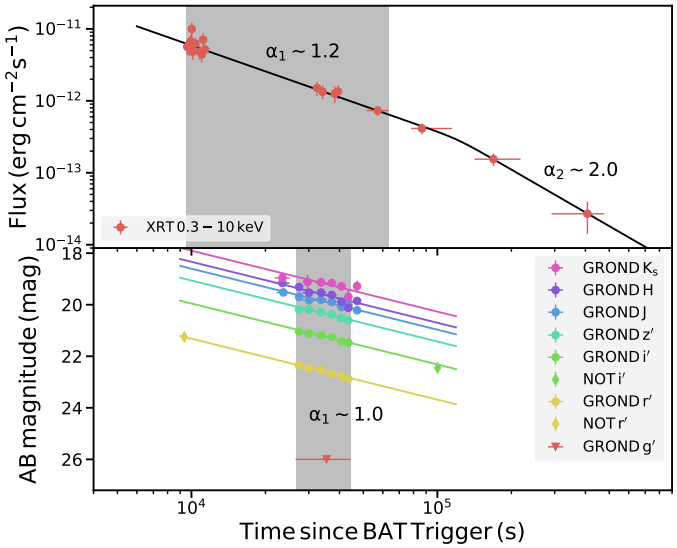

Fig. B.16. GRB 140311A.

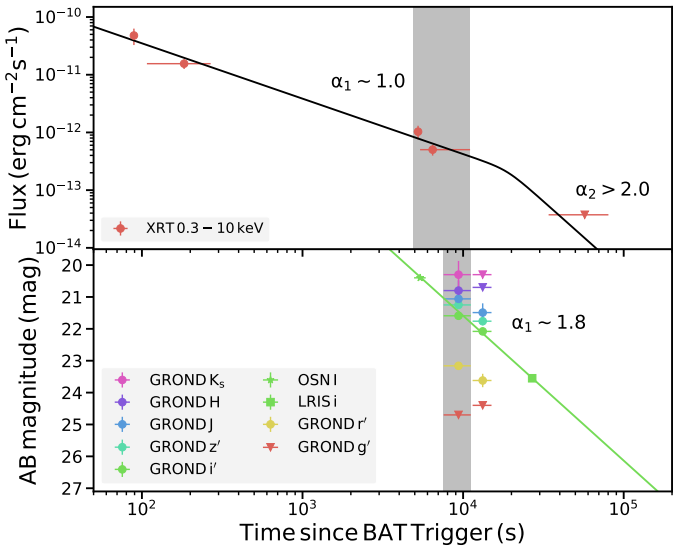

Fig. B.17. GRB 140428A.

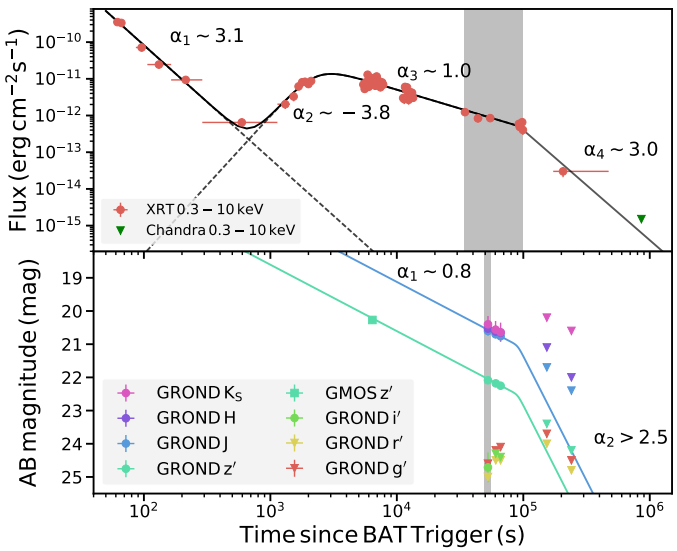

Fig. B.18. GRB 140515A.

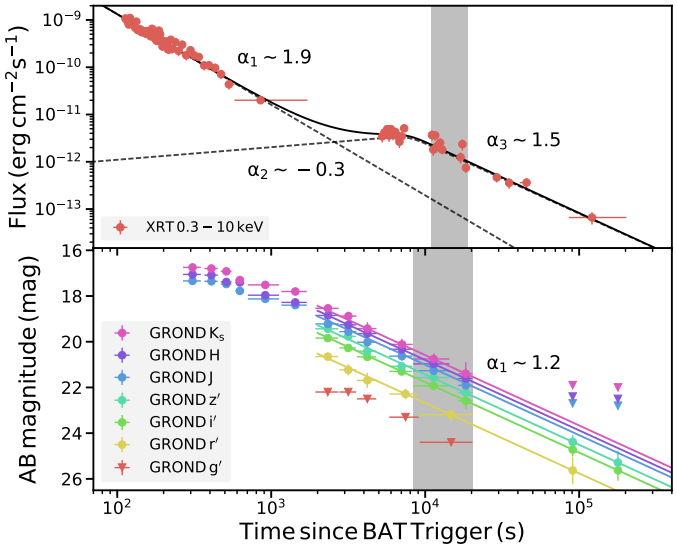

Fig. B.19. GRB 140614A.

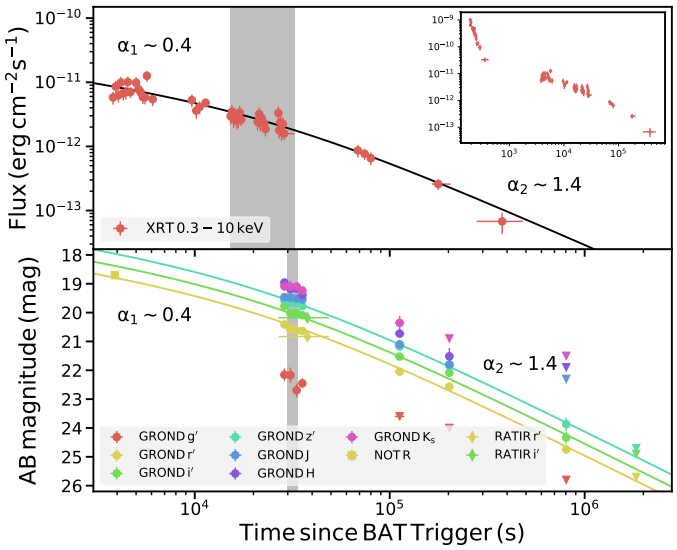

Fig. B.20. GRB 151027B.

Fig. B.21. GRB 151112A.

Appendix C: Additional table and figure

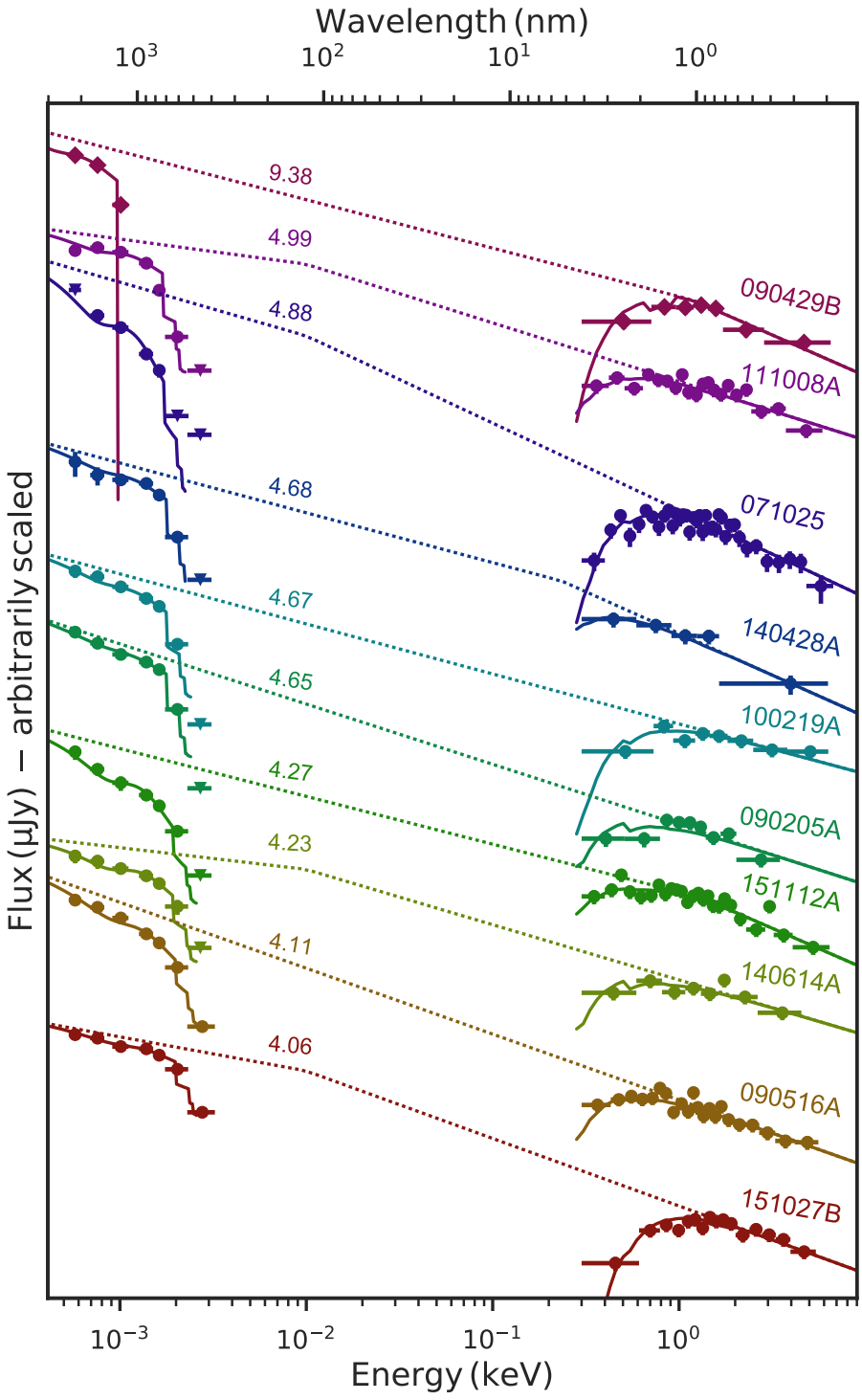

Fig. C.1. Same as Fig. 7, but for the 10 GRBs we additionally fitted with the SN-like dust extinction curve. These GRBs showed evidence of a medium amount of dust ($A_V > 0.1$ mag), when fitted with the local dust extinction curves.

Table C.1. Light curve models and parameters used to flux normalize XRT X-ray and GROND NIR/optical data to a common reference time.

	Model	α_1	α_2	α_3	$t_{\rm break}$ (ks)	Host (y/n)	Additional data[a] (reference)
			GRB 071025				
NIR/opt.	PL	1.32 ± 0.11	...	...	...	no	PAIRTEL $JHK_{\rm s}$ (1)
X-ray	PL	1.60 ± 0.01	...	...	...		
			GRB 080825B[b]				
NIR/opt.	BRPL	1.1 ± 0.1	2.2 ± 0.6	...	59 ± 24	no	DFOSC I (2)
X-ray	PL	1.8 ± 0.6	...	...	...		
			GRB 080913				
NIR/opt.	PL	1.13 ± 0.08	...	...	...	no	
X-ray	PL	1.22 ± 0.06	...	...	...		
			GRB 080916C				
NIR/opt.	PL	1.73 ± 0.39	...	...	...	no	
X-ray	PL	1.30 ± 0.09	...	...	...		
			GRB 090205				
NIR/opt.	PL	1.35 ± 0.04	...	...	...	yes	FORS1 RI (3)
X-ray	BRPL	0.91 ± 0.03	2.12 ± 0.07	...	23 ± 1		
			GRB 090423				
NIR/opt.	BRPL	0.05 ± 0.01	1.00 ± 0.03	...	24 ± 8	no	HAWKI KJ/WFCAM K
X-ray	PL + BRPL	1.38 ± 0.04	−3.75 ± 4.20	1.34 ± 0.15	3.0 ± 4.6		NIRI HJ/ISAAK J (4)(5)
			GRB 090429B[c]				
NIR/opt.	PL	0.61 ± 0.08	...	...	...	no	NIRI JHK (6)
X-ray	BRPL	−1.14 ± 0.59	1.37 ± 0.10	...	0.65 ± 0.18		
			GRB 090516A				
NIR/opt.	PL	1.72 ± 0.05	...	...	...	yes	FORS2 R (7)/NOT R (8)
X-ray	BRPL	0.78 ± 0.06	1.75 ± 0.05	...	16 ± 1		
			GRB 100219A				
NIR/opt.	PL	1.68 ± 0.46	...	...	...	yes	HAWKI KHJ/GMG r'
X-ray	BRPL	1.72 ± 0.25	>3.0	...	...		GTC i' (9)
			GRB 100513A				
NIR/opt.	PL	0.48 ± 0.17	...	...	...	no	PAIRITEL $JHK_{\rm s}$ (10)
X-ray	PL	0.96 ± 0.06	...	...	...		

Notes. [(a)] GROND optical and near-infrared data were extended with data collected from GCNs and refereed publications. The magnitudes were, if necessary, converted to the AB system. [(b)] The XRT light curve is also consistent with the model for the NIR/optical afterglow (see Fig. B.2). [(c)] We used the temporal decay slope as derived from the NIRI K band data to re-scale the NIRI J, H, and K-band observation to a common reference time (see Fig. B.7).

References. (1) Perley et al. (2010); (2) Thoene et al. (2008); (3) D'Avanzo et al. (2010); (4) Tanvir et al. (2009); (5) Salvaterra et al. (2009); (6) Cucchiara et al. (2011); (7) Gorosabel et al. (2009); (8) de Ugarte Postigo et al. (2009); (9) Thöne et al. (2013); (10) Morgan et al. (2010); (11)Hartoog et al. (2015); (12) Castro-Tirado et al. (2013); (13) Butler et al. (2014); (14) Xu et al. (2014b); (15) de Ugarte Postigo et al. (2014); (16) Volnova et al. (2014a); (17) Volnova et al. (2014b); (18) Xu et al. (2014a); (19) Aceituno et al. (2014); (20) Perley (2014a); (21) Melandri et al. (2015); (22) Margutti et al. (2014); (23) Malesani et al. (2015b); (24) Watson et al. (2015a).

Table C.1. continued.

	Model	α_1	α_2	α_3	$t_{\rm break}$ (ks)	Host (y/n)	Additional data[a] (reference)
				GRB 100905A			
NIR/opt.	PL	0.60 ± 0.06	...	...	...	no	
X-ray	PL	0.88 ± 0.03	...	...	...		
				GRB 111008A			
NIR/opt.	PL	1.02 ± 0.06	...	...	...	no	
X-ray	BRPL	0.97 ± 0.09	1.42 ± 0.05	...	41 ± 11		
				GRB 120712A			
NIR/opt.	BRPL	0.04 ± 0.08	1.66 ± 0.16	...	102 ± 13	no	
X-ray	BRPL	0.95 ± 0.03	1.80 ± 0.11	...	6 ± 1		
				GRB 130606A			
NIR/opt.	PL	1.71 ± 0.03	...	...	...	no	NOT $r'i'z'$/TNG $i'z'$ (11)
X-ray	PL	1.71 ± 0.03	...	...	...		GTC $i'z'$ (12)
				GRB 131117A			
NIR/opt.	PL	0.86 ± 0.01	...	...	...	no	
X-ray	PL + G	0.95 ± 0.02	...	...	...		
				GRB 140304A			
NIR/opt.	PL + BRPL	2.25 ± 0.24	−7.42 ± 5.94	1.86 ± 0.20	25 ± 2	no	RATIR *grizJH* (13)
X-ray	PL + BRPL	1.93 ± 0.14	−9.71 ± 6.89	1.50 ± 0.09	16 ± 2		Nanshan *R* (14)/NOT *gr* (15)
							MONDY *R*(16)/ORI-40 *R* (17)
				GRB 140311A			
NIR/opt.	PL	0.95 ± 0.04	...	...	...	no	NOT $r'i'$ (18)
X-ray	BRPL	1.20 ± 0.07	1.97 ± 0.58	...	121 ± 65		
				GRB 140428A			
NIR/opt.	PL	1.81 ± 0.08	...	...	...	no	OSN *I* (19)
X-ray	BRPL	0.96 ± 0.07	>2.0	...	19 ± 9		LRIS *i* (20)
				GRB 140515A			
NIR/opt.	BRPL	0.77 ± 0.25	>2.5	...	...	no	GMOS z' (21)
X-ray	PL + BRPL	3.10 ± 0.19	−3.77 ± 0.69	1.03 ± 0.05	2.3 ± 0.2		Chandra (22)
				GRB 140614A			
NIR/opt.	PL	1.20 ± 0.04	...	...	...	no	
X-ray	PL + BRPL	1.92 ± 0.07	−0.27 ± 0.32	1.49 ± 0.08	7 ± 1		
				GRB 151027B			
NIR/opt.	BRPL	0.44 ± 0.19	1.44 ± 0.14	...	34 ± 28	no	NOT *R* (23)
X-ray	BRPL	0.44 ± 0.19	1.44 ± 0.14	...	34 ± 28		RATIR $r'i'$ (24)
				GRB 151112A			
NIR/opt.	BRPL	0.84 ± 0.06	2.10 ± 0.29	...	128 ± 14	no	
X-ray	BRPL	0.84 ± 0.06	>1.2	...	128 ± 14		

Appendix D: GROND photometry

Table D.1. GROND photometry of the GRB afterglows.

$T_{\rm GROND}$[a]	AB magnitude[b]						
(s)	g'	r'	i'	z'	J	H	$K_{\rm s}$
GRB 071025B/T_0 = 04:08:54 UT (MJD = 54 398.17285) (1)							
80 533 ± 2452	>25.2	>24.5	22.93 ± 0.24	22.29 ± 0.13	21.24 ± 0.18	20.79 ± 0.24	>19.8
GRB 080825B/T_0 = 17:46:40 UT (MJD = 54 703.74074) (2)							
25 566 ± 1670	>24.6	19.78 ± 0.03	18.40 ± 0.03	18.11 ± 0.03	17.76 ± 0.06	17.36 ± 0.05	17.10 ± 0.08
29 344 ± 1670	>24.0	19.91 ± 0.03	18.60 ± 0.03	18.27 ± 0.03	17.94 ± 0.06	17.56 ± 0.06	17.46 ± 0.08
32 695 ± 1431	>24.3	20.05 ± 0.03	18.72 ± 0.03	18.40 ± 0.03	18.02 ± 0.06	17.73 ± 0.06	17.51 ± 0.08
110 261 ± 1981	>24.1	22.22 ± 0.04	20.93 ± 0.04	20.67 ± 0.05	20.17 ± 0.15	19.97 ± 0.14	>18.8
29 201 ± 4779	>24.4	19.94 ± 0.03	18.62 ± 0.03	18.30 ± 0.03	17.92 ± 0.06	17.57 ± 0.05	17.41 ± 0.08
GRB 080913/T_0 = 06:46:54 UT (MJD = 54 722.28257) (3)							
556 ± 193	>22.4	>23.4	>23.0	21.55 ± 0.14	19.88 ± 0.10	19.86 ± 0.16	19.44 ± 0.35
994 ± 189	>23.2	>23.4	>23.0	22.23 ± 0.26	20.59 ± 0.18	20.46 ± 0.27	20.24 ± 0.50
1962 ± 730	>23.8	>24.3	>23.6	23.07 ± 0.27	21.33 ± 0.21	20.88 ± 0.21	20.70 ± 0.39
4326 ± 1542	>24.3	>24.9	>24.0	24.18 ± 0.38	21.95 ± 0.60	21.36 ± 0.39	>20.9
7715 ± 1769	>24.4	>25.1	>24.1	24.81 ± 0.65	>22.3	>21.6	>21.0
GRB 080916C/T_0 = 00:12:45 UT (MJD = 54 725.00885) (4)							
117 308 ± 3045	>24.0	22.80 ± 0.07	22.00 ± 0.05	21.66 ± 0.05	21.45 ± 0.06	21.26 ± 0.08	21.04 ± 0.15
GRB 090205/T_0 = 23:03:14 UT (MJD = 54 867.96058) (5)							
23 348 ± 340	>22.9	22.39 ± 0.14	20.76 ± 0.06	20.48 ± 0.05	20.16 ± 0.13	19.84 ± 0.15	19.25 ± 0.26
24 111 ± 342	>23.1	22.18 ± 0.10	20.75 ± 0.05	20.66 ± 0.05	20.17 ± 0.12	19.66 ± 0.12	19.60 ± 0.29
25 396 ± 860	>24.2	22.43 ± 0.06	20.93 ± 0.04	20.69 ± 0.04	20.49 ± 0.10	19.89 ± 0.09	19.87 ± 0.28
27 201 ± 858	>25.1	22.57 ± 0.05	21.06 ± 0.03	20.78 ± 0.03	20.34 ± 0.09	20.05 ± 0.13	19.70 ± 0.21
120 692 ± 2656	>25.9	24.67 ± 0.13	23.02 ± 0.07	22.60 ± 0.08	>22.6	>22.0	>20.8
207 844 ± 2677	>25.2	25.37 ± 0.47	23.78 ± 0.15	23.35 ± 0.13	>22.5	>21.9	>21.0
25 534 ± 2525	>25.3	22.50 ± 0.04	20.97 ± 0.03	20.64 ± 0.03	20.29 ± 0.07	19.85 ± 0.08	19.42 ± 0.12
GRB 090423/T_0 = 07:55:19 UT (MJD= 54 944.33008) (6)							
62 136 ± 7076	>25.0	>25.1	>24.2	>24.0	21.61 ± 0.11	21.19 ± 0.11	20.89 ± 0.12
150 527 ± 3557	>24.6	>24.8	>24.7	>23.2	>22.5	>21.9	>21.1
GRB 090429B/T_0 = 05:30:03 UT (MJD= 54 950.22920) (7)							
1902 ± 1081	>23.7	>23.5	>22.8	>22.3	>20.9	>20.3	>19.8
81 805 ± 3629	>25.7	>25.4	>24.6	>24.0	>22.3	>21.8	>20.7
GRB 090516/T_0 = 08:27:50 UT (MJD= 54 967.35266) (8)							
53 290 ± 724	23.86 ± 0.14	21.34 ± 0.03	20.39 ± 0.04	19.89 ± 0.04	19.63 ± 0.10	19.29 ± 0.10	19.16 ± 0.16
54 959 ± 859	23.76 ± 0.10	21.40 ± 0.03	20.41 ± 0.03	19.96 ± 0.03	19.54 ± 0.08	19.17 ± 0.09	19.04 ± 0.13
56 764 ± 861	24.04 ± 0.13	21.43 ± 0.03	20.43 ± 0.03	20.01 ± 0.03	19.57 ± 0.08	19.20 ± 0.10	18.99 ± 0.14
58 112 ± 175	>23.6	21.43 ± 0.06	20.47 ± 0.05	20.11 ± 0.05	19.84 ± 0.14	19.23 ± 0.16	19.18 ± 0.23
65 203 ± 862	23.90 ± 0.29	21.60 ± 0.04	20.62 ± 0.03	20.17 ± 0.04	19.85 ± 0.09	19.42 ± 0.10	18.88 ± 0.14

Notes. [a] Mid-time of the GROND exposure in seconds after the detection of the prompt emission (T_0). [b] Magnitudes are not corrected for the Galactic foreground extinction given in Table 1. Upper limits are 3σ. Below the dashed lines we give the magnitudes of stacked observations. Empty entries (...) indicate technical problems, reflections rings at the position of the source, or when we used the magnitudes of stacked/single observations instead.

References. (1) Pagani et al. (2007); (2) Evangelista et al. (2008); (3) Schady et al. (2008); (4) Goldstein & van der Horst (2008); (5) Perri et al. (2009); (6) Krimm et al. (2009); (7) Ukwatta et al. (2009); (8) Rowlinson et al. (2009); (9) Rowlinson et al. (2010); (10) Mereghetti et al. (2010); (11) Marshall et al. (2010); (12) Saxton et al. (2011); (13) Page et al. (2012); (14) Yershov et al. (2012); (15) Ukwatta et al. (2013); (16) Page et al. (2013); (17) Racusin et al. (2014); (18) Kocevski et al. (2014); (19) D'Avanzo et al. (2014); (20) Page et al. (2014); (21) Ukwatta et al. (2015); (22) Malesani et al. (2015a).

Table D.1. continued.

$T_{\mathrm{GROND}}{}^{a}$	AB magnitude[b]						
(s)	g'	r'	i'	z'	J	H	K_{s}
143 076 ± 859	25.28 ± 0.29	23.15 ± 0.06	21.99 ± 0.05	21.67 ± 0.06	21.00 ± 0.15	20.75 ± 0.20	20.01 ± 0.25
229 907 ± 859	>25.3	23.94 ± 0.15	22.72 ± 0.09	22.41 ± 0.13	>21.8	>21.1	>20.3
487 152 ± 3319	>26.0	24.78 ± 0.15	23.53 ± 0.13	23.00 ± 0.15	>22.3	>21.8	>20.9
55 095 ± 2530	23.87 ± 0.07	21.40 ± 0.03	20.41 ± 0.03	19.92 ± 0.03	19.61 ± 0.07	19.18 ± 0.07	19.00 ± 0.10
GRB 100219A/T_0 = 15:15:46 (MJD = 55 246.63606) (9)							
34 248 ± 1130	>24.2	22.77 ± 0.09	21.37 ± 0.06	21.24 ± 0.08	20.72 ± 0.20	20.23 ± 0.19	20.12 ± 0.34
41 043 ± 2656	>26.0	23.17 ± 0.05	21.73 ± 0.04	21.40 ± 0.04	20.92 ± 0.12	20.53 ± 0.13	20.31 ± 0.23
131 666 ± 2672	>26.1	24.52 ± 0.12	23.62 ± 0.10	23.54 ± 0.15	>22.3	>21.7	>20.8
221 279 ± 2528	>25.9	24.68 ± 0.14	23.98 ± 0.15	22.84 ± 0.20	>22.4	>21.9	>20.9
397 579 ± 3575	>25.8	24.83 ± 0.17	24.69 ± 0.27	24.34 ± 0.32	>22.5	>22.1	>20.6
GRB 100518A/T_0 = 11:33:35 UT (MJD = 55 334.48166) (10)							
71 558 ± 9906	25.57 ± 0.57	23.74 ± 0.13	23.27 ± 0.18	22.94 ± 0.17	22.20 ± 0.42	21.53 ± 0.37	>20.3
GRB 100905A/T_0 = 15:08:14 UT (MJD = 55 444.63072) (11)							
57 687 ± 9809	>25.9	>26.1	>25.2	>24.7	21.85 ± 0.20	21.72 ± 0.26	21.50 ± 0.43
GRB 111008A/T_0 = 22:12:58 UT (MJD = 55 842.92567) (12)							
24 653 ± 1512	>24.4	22.76 ± 0.09	21.03 ± 0.04	20.00 ± 0.03	19.58 ± 0.06	19.42 ± 0.07	19.23 ± 0.10
28 944 ± 2675	>24.7	23.11 ± 0.09	21.14 ± 0.04	20.18 ± 0.03	19.74 ± 0.06	19.58 ± 0.08	19.53 ± 0.14
34 402 ± 2682	>25.1	23.21 ± 0.09	21.36 ± 0.04	20.30 ± 0.03	19.92 ± 0.06	19.95 ± 0.10	19.79 ± 0.15
116 116 ± 1762	>23.9	>24.2	22.56 ± 0.11	21.60 ± 0.06	20.99 ± 0.15	20.92 ± 0.25	20.38 ± 0.28
207 405 ± 3588	>23.9	24.45 ± 0.26	22.67 ± 0.16	22.21 ± 0.11	21.37 ± 0.16	20.94 ± 0.18	20.60 ± 0.28
293 685 ± 3582	>23.9	>24.3	23.30 ± 0.20	22.09 ± 0.11	21.80 ± 0.17	21.30 ± 0.18	20.83 ± 0.24
639 133 ± 3576	>24.7	>24.2	24.35 ± 0.34	23.87 ± 0.27	>22.6	>22.0	>21.1
982 066 ± 1771	>25.4	>25.4	>24.8	>24.1	>22.4	>21.7	>20.7
GRB 120712A/T_0 = 13:42:27 UT (MJD = 56 120.57115) (13)							
34 495 ± 1191	23.24 ± 0.09	21.26 ± 0.03	20.58 ± 0.04	20.44 ± 0.04	20.02 ± 0.09	19.90 ± 0.11	19.67 ± 0.18
37 541 ± 1771	23.11 ± 0.06	21.27 ± 0.03	20.61 ± 0.03	20.34 ± 0.03	20.12 ± 0.08	19.78 ± 0.10	19.89 ± 0.22
41 032 ± 1633	23.17 ± 0.07	21.28 ± 0.03	20.63 ± 0.03	20.38 ± 0.04	19.97 ± 0.08	19.95 ± 0.11	19.34 ± 0.17
297 391 ± 2680	25.44 ± 0.37	23.21 ± 0.07	22.50 ± 0.08	22.44 ± 0.14	>21.9	>21.3	>20.7
470 194 ± 2447	>25.2	24.27 ± 0.16	23.25 ± 0.15	...	>22.1	>21.4	>20.0
641 263 ± 1767	>25.4	24.55 ± 0.19	23.80 ± 0.22	>23.7	>21.9	>21.4	>20.1
37 984 ± 4681	23.17 ± 0.05	21.28 ± 0.03	20.62 ± 0.03	20.42 ± 0.03	20.03 ± 0.07	19.86 ± 0.08	19.71 ± 0.14
GRB 120923A/T_0 = 05:16:06 UT (MJD = 56 193.21951) (14)							
72 311 ± 4059	>23.8	>24.3	>23.7	>23.7	>22.1	>21.7	>20.7
GRB 130606A/T_0 = 21:04:39 UT (MJD = 56 449.87823) (15)							
24 785 ± 1650	>25.2	23.46 ± 0.09	...	...	18.28 ± 0.05	17.95 ± 0.05	17.77 ± 0.13
30 132 ± 1937	>25.0	24.05 ± 0.17	21.46 ± 0.05	18.99 ± 0.03	18.56 ± 0.05	18.30 ± 0.06	18.05 ± 0.08
114 988 ± 4498	>25.5	>25.0	...	21.56 ± 0.06	20.73 ± 0.13	20.58 ± 0.26	20.42 ± 0.25
GRB 131117A/T_0 = 00:34:04 UT (MJD = 56 613.02366) (16)							
218 ± 33	...	18.37 ± 0.03	17.91 ± 0.03	17.70 ± 0.04	...	...	...
418 ± 33	...	19.04 ± 0.04	18.60 ± 0.04	18.43 ± 0.04	...	...	...
520 ± 33	...	19.26 ± 0.04	18.80 ± 0.04	18.62 ± 0.05	...	...	...
629 ± 33	...	19.39 ± 0.04	18.94 ± 0.04	18.84 ± 0.04	...	...	...
730 ± 33	...	19.63 ± 0.04	...	18.85 ± 0.21	...	...	...
840 ± 33	...	19.67 ± 0.05	19.22 ± 0.04	19.16 ± 0.04	...	...	...
951 ± 33	...	19.86 ± 0.05	19.34 ± 0.04	19.19 ± 0.04	...	...	...
1087 ± 57	...	20.06 ± 0.04	19.46 ± 0.04	19.21 ± 0.04	...	...	...

Table D.1. continued.

T_{GROND}[a]	AB magnitude[b]						
(s)	g'	r'	i'	z'	J	H	K_s
1276 ± 57	...	19.99 ± 0.04	...	19.60 ± 0.22	...	...	...
1472 ± 57	...	20.13 ± 0.04	19.66 ± 0.05	19.47 ± 0.05	...	...	...
1668 ± 57	...	20.26 ± 0.05	19.86 ± 0.05	19.53 ± 0.05	...	...	...
1871 ± 57	...	20.39 ± 0.05	19.90 ± 0.05	19.73 ± 0.04	...	...	...
369 ± 184	20.15 ± 0.05	18.82 ± 0.03	18.40 ± 0.03	18.19 ± 0.04	18.18 ± 0.06	17.97 ± 0.06	17.80 ± 0.11
790 ± 194	20.94 ± 0.09	...	...	...	18.96 ± 0.08	18.79 ± 0.08	18.50 ± 0.20
1378 ± 348	21.17 ± 0.08	...	...	...	19.42 ± 0.08	19.29 ± 0.10	>18.7
GRB 140311A/T_0 = 21:05:16 UT (MJD = 56 727.87866) (17)							
27 387 ± 865	>23.9	22.36 ± 0.07	21.04 ± 0.04	20.18 ± 0.03	19.70 ± 0.07	19.31 ± 0.09	18.96 ± 0.21
30 065 ± 1727	>23.9	22.47 ± 0.05	21.11 ± 0.03	20.19 ± 0.03	19.83 ± 0.06	19.53 ± 0.09	...
33 620 ± 1733	>24.2	22.55 ± 0.05	21.19 ± 0.03	20.29 ± 0.03	19.81 ± 0.06	19.53 ± 0.08	19.13 ± 0.18
37 169 ± 1734	>25.7	22.68 ± 0.04	21.25 ± 0.03	20.38 ± 0.03	19.90 ± 0.06	19.62 ± 0.08	19.16 ± 0.16
40 733 ± 1739	>25.5	22.78 ± 0.04	21.42 ± 0.03	20.52 ± 0.03	20.08 ± 0.07	19.88 ± 0.09	19.28 ± 0.18
43 437 ± 881	>25.0	22.88 ± 0.07	21.47 ± 0.04	20.61 ± 0.04	20.02 ± 0.09	20.12 ± 0.15	19.70 ± 0.32
47 144 ± 1219	NIR only				20.22 ± 0.11	19.85 ± 0.14	19.28 ± 0.22
35 420 ± 8898	>26.0	22.64 ± 0.03	21.24 ± 0.03	20.32 ± 0.03	19.87 ± 0.05	19.60 ± 0.06	19.27 ± 0.11
GRB 140428A/T_0 = 22:40:50 UT (MJD = 56 775.94502) (18)							
9363 ± 1800	>24.7	23.16 ± 0.12	21.59 ± 0.07	21.15 ± 0.08	21.06 ± 0.24	20.80 ± 0.32	20.30 ± 0.43
13 242 ± 1782	>24.4	23.62 ± 0.21	22.08 ± 0.11	21.76 ± 0.13	21.49 ± 0.29	>20.7	>20.4
618 771 ± 1907	>23.9	>23.7	>23.2	>23.2	>21.6	>21.1	>20.1
GRB 140515A/T_0 = 09:12:36 UT (MJD = 56 792.38375) (19)							
52 538 ± 3000	>24.6	>25.0	24.71 ± 0.45	22.09 ± 0.06	20.60 ± 0.14	20.53 ± 0.18	20.40 ± 0.25
60 572 ± 2435	>24.2	>24.5	>24.3	22.18 ± 0.06	20.70 ± 0.11	20.62 ± 0.15	20.56 ± 0.26
66 119 ± 2693	>24.1	>24.5	>24.4	22.25 ± 0.07	20.76 ± 0.11	20.65 ± 0.14	20.64 ± 0.29
153 522 ± 1787	>23.7	>24.0	>23.5	>23.4	>21.7	>21.1	>20.2
240 133 ± 3814	>24.5	>24.8	>24.5	>24.2	>22.4	>22.0	>20.6
GRB 140614A/T_0 = 01:04:59 UT (MJD = 56 822.04513) (20)							
2331 ± 396	>22.2	20.65 ± 0.13	19.84 ± 0.06	19.43 ± 0.06	19.22 ± 0.14	18.85 ± 0.14	18.54 ± 0.15
3165 ± 394	>22.2	21.23 ± 0.25	20.27 ± 0.10	19.77 ± 0.07	19.56 ± 0.23	19.26 ± 0.20	18.88 ± 0.19
4209 ± 605	>22.5	21.69 ± 0.33	20.66 ± 0.11	20.42 ± 0.11	20.02 ± 0.25	19.64 ± 0.23	19.43 ± 0.28
7038 ± 1203	...	...	21.30 ± 0.10	21.08 ± 0.11	20.63 ± 0.20	20.33 ± 0.20	20.12 ± 0.25
11 337 ± 2973	...	...	21.93 ± 0.10	21.57 ± 0.12	21.27 ± 0.18	20.97 ± 0.25	20.76 ± 0.24
18 358 ± 1916	...	...	22.58 ± 0.38	22.23 ± 0.33	21.90 ± 0.35	21.61 ± 0.39	21.40 ± 0.50
90 787 ± 3616	>25.1	25.63 ± 0.60	24.72 ± 0.28	24.38 ± 0.29	>22.7	>22.4	>21.9
178 637 ± 4062	>25.3	>25.6	25.63 ± 0.45	25.29 ± 0.52	>22.8	>22.5	>20.0
7453 ± 1617	>23.3	22.29 ± 0.24	...	...	...	...	...
14 747 ± 5527	>24.4	23.19 ± 0.27	...	...	...	...	...
GRB 151027B/T_0 = 22:40:40 UT (MJD = 57 322.94491) (21)							
28 839 ± 903	22.16 ± 0.23	20.41 ± 0.05	19.78 ± 0.04	19.58 ± 0.04	19.47 ± 0.09	18.96 ± 0.08	19.09 ± 0.16
30 948 ± 1125	22.17 ± 0.26	20.59 ± 0.07	20.02 ± 0.06	19.66 ± 0.05	19.48 ± 0.10	19.19 ± 0.10	19.10 ± 0.20
33 291 ± 1129	22.69 ± 0.24	20.62 ± 0.04	20.00 ± 0.04	19.67 ± 0.04	19.52 ± 0.07	19.17 ± 0.08	19.10 ± 0.14

Table D.1. continued.

$T_{\rm GROND}$[a]	AB magnitude[b]						
(s)	g'	r'	i'	z'	J	H	$K_{\rm s}$
35 634 ± 1130	22.45 ± 0.16	20.64 ± 0.04	20.09 ± 0.04	19.77 ± 0.04	19.54 ± 0.07	19.39 ± 0.08	19.24 ± 0.14
112 431 ± 6317	>23.6	22.05 ± 0.07	21.53 ± 0.07	21.18 ± 0.06	21.10 ± 0.15	20.73 ± 0.16	20.36 ± 0.24
202 273 ± 1606	>24.0	22.57 ± 0.09	22.09 ± 0.09	21.85 ± 0.08	21.80 ± 0.25	21.53 ± 0.29	>20.9
804 300 ± 6436	>25.8	24.75 ± 0.16	24.33 ± 0.21	23.87 ± 0.23	>22.3	>21.9	>21.5
31 733 ± 2686	22.46 ± 0.16	20.60 ± 0.04	19.98 ± 0.04	19.66 ± 0.04	19.47 ± 0.07	19.11 ± 0.07	18.95 ± 0.11
GRB 151112A/T_0 = 13:44:48 UT (MJD = 57 338.57278) (22)							
41 030 ± 3474	>25.4	23.58 ± 0.09	22.63 ± 0.08	22.23 ± 0.09	21.74 ± 0.26	21.25 ± 0.22	20.59 ± 0.26
130 717 ± 2389	>25.7	24.56 ± 0.14	23.63 ± 0.12	23.50 ± 0.20	>22.3	>21.8	>20.8
225 119 ± 2393	>25.2	>25.0	>24.3	>23.7	>22.0	>21.6	>20.6